SPECTRAL AND MORPHOLOGICAL ANALYSIS OF THE REMNANT OF SUPERNOVA 1987A WITH ALMA AND ATCA

GIOVANNA ZANARDO[1], LISTER STAVELEY-SMITH[1,2], REMY INDEBETOUW[3,4], ROGER A. CHEVALIER[3],
MIKAKO MATSUURA[5], BRYAN M. GAENSLER[2,6], MICHAEL J. BARLOW[5], CLAES FRANSSON[7], RICHARD N. MANCHESTER[8],
MAARTEN BAES[9], JULIA R. KAMENETZKY[10], MAŠA LAKIĆEVIĆ[11], PETER LUNDQVIST[7], JON M. MARCAIDE[12,13],
IVAN MARTÍ-VIDAL[14], MARGARET MEIXNER[15,16], C.-Y. NG[17], SANGWOOK PARK[18], GEORGE SONNEBORN[19],
JASON SPYROMILIO[20], AND JACCO TH. VAN LOON[11]

[1] International Centre for Radio Astronomy Research (ICRAR), M468, University of Western Australia, Crawley, WA 6009, Australia; giovanna.zanardo@gmail.com
[2] Australian Research Council, Centre of Excellence for All-sky Astrophysics (CAASTRO)
[3] Department of Astronomy, University of Virginia, P.O. Box 400325, Charlottesville, VA 22904, USA
[4] National Radio Astronomy Observatory (NRAO), 520 Edgemont Road, Charlottesville, VA 22903, USA
[5] Department of Physics and Astronomy, University College London, Gower Street, London WC1E 6BT, UK
[6] Sydney Institute for Astronomy, School of Physics, University of Sydney, NSW 2006, Australia
[7] Department of Astronomy, Oskar Klein Center, Stockholm University, AlbaNova, SE-106 91 Stockholm, Sweden
[8] CSIRO Astronomy and Space Science, Australia Telescope National Facility, P.O. Box 76, Epping, NSW 1710, Australia
[9] Sterrenkundig Observatorium, Universiteit Gent, Krijgslaan 281 S9, B-9000 Gent, Belgium
[10] Steward Observatory, University of Arizona, 933 North Cherry Avenue, Tucson, AZ 85721-0065, USA
[11] Institute for the Environment, Physical Sciences and Applied Mathematics, Lennard-Jones Laboratories, Keele University, Staffordshire ST5 5BG, UK
[12] Departamento de Astronomía, Universidad de Valencia, C/Dr. Moliner 50, E-46100 Burjassot, Spain
[13] Donostia International Physics Center, Paseo de Manuel de Lardizabal 4, E-20018 Donostia-San Sebastian, Spain
[14] Department of Earth and Space Sciences, Chalmers University of Technology, Onsala Space Observatory, SE-439 92 Onsala, Sweden
[15] Space Telescope Science Institute, 3700 San Martin Drive, Baltimore, MD 21218, USA
[16] Department of Physics and Astronomy, Johns Hopkins University, 366 Bloomberg Center, 3400 North Charles Street, Baltimore, MD 21218, USA
[17] Department of Physics, University of Hong Kong, Pokfulam Road, Hong Kong, China
[18] Department of Physics, University of Texas at Arlington, 108 Science Hall, Box 19059, Arlington, TX 76019, USA
[19] NASA Goddard Space Flight Center, 8800 Greenbelt Road, Greenbelt, MD 20771, USA
[20] European Southern Observatory (ESO), Karl-Schwarzschild-Str. 2, D-85748 Garching b. München, Germany

ABSTRACT

We present a comprehensive spectral and morphological analysis of the remnant of supernova (SN) 1987A with the Australia Telescope Compact Array (ATCA) and the Atacama Large Millimeter/submillimeter Array (ALMA). The non-thermal and thermal components of the radio emission are investigated in images from 94 to 672 GHz (λ 3.2 mm to 450 μm), with the assistance of a high-resolution 44 GHz synchrotron template from the ATCA, and a dust template from ALMA observations at 672 GHz. An analysis of the emission distribution over the equatorial ring in images from 44 to 345 GHz highlights a gradual decrease of the east-to-west asymmetry ratio with frequency. We attribute this to the shorter synchrotron lifetime at high frequencies. Across the transition from radio to far infrared, both the synchrotron/dust-subtracted images and the spectral energy distribution (SED) suggest additional emission beside the main synchrotron component ($S_\nu \propto \nu^{-0.73}$) and the thermal component originating from dust grains at $T \sim 22$ K. This excess could be due to free–free flux or emission from grains of colder dust. However, a second flat-spectrum synchrotron component appears to better fit the SED, implying that the emission could be attributed to a pulsar wind nebula (PWN). The residual emission is mainly localized west of the SN site, as the spectral analysis yields $-0.4 \lesssim \alpha \lesssim -0.1$ across the western regions, with $\alpha \sim 0$ around the central region. If there is a PWN in the remnant interior, these data suggest that the pulsar may be offset westward from the SN position.

Key words: ISM: supernova remnants – radiation mechanisms: non-thermal – radiation mechanisms: thermal – radio continuum: general – stars: neutron – supernovae: individual (SN 1987A)

Online-only material: color figures

1. INTRODUCTION

The evolution of the remnant of supernova (SN) 1987A in the Large Magellanic Cloud has been closely monitored since the collapse of its progenitor star, Sanduleak (Sk) $-69°202$, on 1987 February 23. Models of Sk $-69°202$ indicated that it had an initial mass of $\sim 20\,M_\odot$ (Hillebrandt et al. 1987). The mass range of the progenitor is consistent with the formation of a neutron star (NS; Thielemann & Arnett 1985), and thus with the neutrino events reported by the Kamioka NDE (Hirata et al. 1987) and IMB (Bionta et al. 1987; Haines et al. 1988) detectors. Models by Crotts & Heathcote (2000) suggest a transition from red supergiant into blue supergiant to explain

the hourglass nebula structure, which envelopes the SN with three nearly stationary rings (Chevalier & Dwarkadas 1995; Blondin & Lundqvist, 1993; Martin & Arnett 1995; Morris & Podsiadlowski 2007). The two outer rings, imaged with the *Hubble Space Telescope* (*HST*; Jakobsen et al. 1991; Plait et al. 1995), are located on either side of the central ring in the equatorial plane (equatorial ring, ER), and likely formed at the same time as the ER (Crotts & Heathcote 2000; Tziamtzis et al. 2011). The synchrotron emission, generated by the shock propagating into the clumpy circumstellar medium (CSM) close to the equatorial plane, was detected in the mid-1990s (Turtle et al. 1990; Staveley-Smith et al. 1992), and has become brighter over time (Manchester et al. 2002; Zanardo et al. 2010). Radio

observations have stretched from flux monitoring at 843 MHz with the Molonglo Observatory Synthesis Telescope (Staveley-Smith et al. 1993; Ball et al. 2001) to images of sub-arcsec resolution with the Australia Telescope Compact Array (ATCA; Gaensler et al. 1997; Manchester et al. 2005a; Ng et al. 2008; Potter et al. 2009; Zanardo et al. 2013). ATCA observations at 94 GHz (Lakićević et al. 2012b) have been followed by observations from 100 GHz up to 680 GHz with the Atacama Large Millimeter/submillimeter Array (ALMA; Kamenetzky et al. 2013; Indebetouw et al. 2014).

The ongoing shock expansion has been monitored at 9 GHz since 1992 (Gaensler et al. 1997, 2007). Shock velocities of ∼4000 km s^{-1} have been measured between day 4000 and 7000 (Ng et al. 2008), while signs of a slower expansion have been tentatively detected after day ∼7000, as the shock has likely propagated past the high-density CSM in the ER (Ng et al. 2013). Similar evidence of slower shock expansion since day ∼6000 has been found in X-ray data (Park et al. 2005, 2006; Racusin et al. 2009) as well as in infrared (IR) data (Bouchet et al. 2006).

Since the early super-resolved images at 9 GHz (Gaensler et al. 1997), a limb-brightened shell morphology has been characteristic of the remnant. The radio emission, over the years, has become more similar to an elliptical ring rather than the original truncated-shell torus (Ng et al. 2013). The radio remnant has shown a consistent east–west asymmetry peaking on the eastern lobe, which has been associated with higher expansion velocities of the eastbound shocks (Zanardo et al. 2013). The asymmetry degree appears to have changed with the shock expansion, as images at 9 GHz exhibit a decreasing trend in the east–west asymmetry since day ∼7000 (Ng et al. 2013). High-resolution observations at 1.4–1.6 GHz (Ng et al. 2011) via Very Long Baseline Interferometry (VLBI) with the Australian Large Baseline Array (LBA) have highlighted the presence of small-scale structures in the brightest regions in both lobes.

The relation between the radio emission and the synchrotron spectral indices, α ($S_\nu \propto \nu^\alpha$), has been investigated via both flux monitoring (Manchester et al. 2002; Zanardo et al. 2010) and imaging observations (Potter et al. 2009; Lakićević et al. 2012b; Zanardo et al. 2013) with the ATCA. The progressive flattening of the radio spectrum derived from 843 MHz to 8.6 GHz at least since day 5000, coupled with the e-folding rate of the radio emission, has pointed to an increasing production of non-thermal electrons and cosmic rays (CR) by the shock front (Zanardo et al. 2010). On the other hand, the association of steeper spectral indices with the brightest eastern sites implies a higher injection efficiency on the eastern side of the supernova remnant (SNR; Zanardo et al. 2013). Flatter spectral indices in the center of the remnant have been tentatively identified from low-resolution two-frequency spectral maps (Potter et al. 2009; Lakićević et al. 2012b), while at 18–44 GHz the central and center–north regions have $-0.5 \lesssim \alpha \lesssim -0.3$ (Zanardo et al. 2013). With ALMA, the spectral energy distribution (SED) of the remnant has been mapped where the non-thermal and thermal components of the emission overlap, identifying cold dust in the SNR interior (Indebetouw et al. 2014), which accommodates 0.4–0.7 $M_\odot$ of the dust mass discovered with the *Herschel Space Observatory* (*Herschel*; Matsuura et al. 2011) in the ejecta.

This paper combines the results presented by Indebetouw et al. (2014) with a comprehensive morphological and spectral analysis of SNR 1987A based on both ATCA and ALMA data.

In Section 2, we present the ALMA Cycle 0 super-resolved images before and after subtraction, in the Fourier plane, of the synchrotron and dust components (Section 3). In Section 4, we assess the remnant asymmetry from 44 to 345 GHz. In Section 5, we update the SED derived by Indebetouw et al. (2014), while, in Section 6, we investigate the spectral index variations in the SNR across the transition from radio to far infrared (FIR). In Section 7, we discuss possible particle flux injection by a pulsar situated in the inner regions of the remnant.

2. OBSERVATIONS AND ANALYSIS

The ATCA and ALMA observations used in this study were performed in 2011 and 2012. ATCA observations at 44 and 94 GHz are detailed in Zanardo et al. (2013) and Lakićević et al. (2012b), respectively. ALMA observations were made in 2012 (Cycle 0) from April to November, over four frequency bands: Band 3 (B3, 84–116 GHz, λ 3 mm), Band 6 (B6, 211–275 GHz, λ 1.3 mm), Band 7 (B7, 275–373 GHz, λ 850 μm), and Band 9 (B9, 602–720 GHz, λ 450 μm). Each band was split over dual 2 GHz wide sidebands, with minimum baselines of 17 m (B9) to maximum baselines of 400 m (B3). All observations used quasars J0538-440 and J0637-752 as bandpass and phase calibrators, respectively. Callisto was observed as an absolute flux calibrator in B3 and B6, while Ceres was used in B7 and B9 (see also Kamenetzky et al. 2013). It is noted that, while ALMA is designed to yield data with flux density calibration uncertainty as low as ∼1%, in Cycle 0 this uncertainty is estimated at ∼5% at all frequencies. Relevant observational parameters are listed in Table 1 (see also Table 1 in Indebetouw et al. 2014).

Each data set was calibrated with the CASA[21] package, then exported in MIRIAD[22] for imaging. After CLEAN-ing (Högbom 1974), both phase and amplitude self-calibration were applied in B3 over a 2 minute solution interval, while only phase calibration was applied in B6 and B7. No self-calibration was performed in B9. As in Zanardo et al. (2013), we note that since the self-calibration technique removes position information, each image was compared with that prior to self-calibration and, in case of positional changes, the self-calibrated images were shifted. Further adjustments were made in the comparison with the ATCA observations at 44 GHz, based on prominent features on the eastern lobe and location of the remnant center. As from Zanardo et al. (2013), the 44 GHz image was aligned with VLBI observations of the SNR (G. Zanardo et al., in preparation). Adding in quadrature these positional uncertainties and the accuracy of the LBA VLBI frame, the errors in the final image position are estimated at ∼60 mas.

Deconvolution was carried out via the maximum entropy method (MEM; Gull & Daniell 1978) in B3, B6, and B7. A weighting parameter of robust = 0.5 (Briggs 1995) was used in all bands. The resultant diffraction-limited images, which have central frequency at 102 GHz in B3, 213 GHz in B6, 345 GHz in B7, and 672 GHz in B9, were then super-resolved with a circular beam of 0″.8 in B3, 0″.6 in B6, and 0″.3 in B7 and B9. The diffraction limited and super-resolved images are shown in the first column of Figures 1 and 2, below the ATCA image at 94 GHz (Lakićević et al. 2012b). Integrated Stokes *I* flux densities, dynamic range and related rms are given in Table 2.

To decouple the non-thermal emission from that originating from dust, the synchrotron component, as resolved with ATCA at 44 GHz (Zanardo et al. 2013), and the dust component, as

---

[21] http://casa.nrao.edu/

[22] http://www.atnf.csiro.au/computing/software/miriad/

Table 1
ALMA Observing Parameters

Parameter	102 GHz (Band 3, B3)	213 GHz (Band 6, B6)	345 GHz (Band 7, B7)	672 GHz (Band 9, B9)
Date (2012)	Apr 5, 6	Jul 15 and Aug 10	Jul 14 and Aug 24	Aug 25and Nov 5
Day since explosion	9174	9287	9294	9351
Frequency bands[a](GHz)	100.093–101.949	213.506–213.597	336.979–340.917	661.992–665.992
	102.051–103.907		349.010–352.963	678.008–682.008
Center frequency (GHz)	101.918	213.146	345.364	672.165
Channel width (MHz)	4.883	4.883	31.250	15.625
Max baselines (u, v) (kλ)	150, 120	180, 260	400, 400	700, 700
No. of antennas	14–18	14–23	28	19–25
Total observing time (hr)	0.83	1.03	0.62	3.40

Note. [a] In B3 and B6, the frequency range is selected to avoid CO and SiO emission (Kamenetzky et al. 2013).

Table 2
Image Parameters

Image (GHz)	S_ν[a] (mJy)	SR Beam[b] ($''$)	DL Beam[c] ($''$)	P.A. ($°$)	Rms Noise (mJy beam^{-1})	Dynamic Range
94[d]	24.2 ± 3.9	0.7	⋯	⋯	0.085	137
102[e]	23.1 ± 3.1	0.8	1.74×1.25	5.7	0.033	285
213	19.7 ± 1.6	0.6	1.16×0.74	-68.5	0.034	75
345	16.7 ± 1.5	0.3	0.65×0.48	-40.2	0.023	121
672	52.8 ± 14.2	0.3	0.34×0.28	68.5	1.219	28
$94-I_{B9}$[f]	23.2 ± 3.9	0.7	0.78×0.63	15.4	0.094	81
$102-I_{B9}$	19.4 ± 3.2	0.8	1.66×1.19	6.3	0.034	143
$213-I_{B9}$	16.9 ± 1.9	0.6	1.16×0.74	-68.5	0.029	64
$345-I_{B9}$	11.5 ± 1.9	0.3	0.65×0.48	-44.0	0.031	43
$672-I_{B9}$	-1.0 ± 14.3	0.3	0.34×0.28	68.5	1.193	2
$94-I_{44}$[g]	0.9 ± 3.9	0.7	0.78×0.63	15.4	0.095	60
$102-I_{44}$	3.5 ± 3.1	0.8	1.48×0.96	10.1	0.027	81
$213-I_{44}$	2.9 ± 1.7	0.6	1.16×0.74	-68.5	0.024	26
$345-I_{44}$	5.8 ± 1.6	0.3	0.65×0.48	-44.0	0.014	90
$672-I_{44}$	47.4 ± 14.8	0.3	0.57×0.55	78.6	0.816	24

Notes.
[a] All flux densities are derived from the diffraction-limited images. The errors are derived from the flux calibration uncertainty combined with the uncertainties in the image subtraction.
[b] Circular beam used for super-resolution (SR).
[c] Beam associated with the diffraction-limited (DL) image.
[d] The flux density is scaled to day 9280 via exponential fitting parameters derived for ATCA flux densities from day 8000, as measured at 8.6 and 9 GHz (G. Zanardo et al., in preparation). All other image parameters are as from Lakićević et al. (2012b).
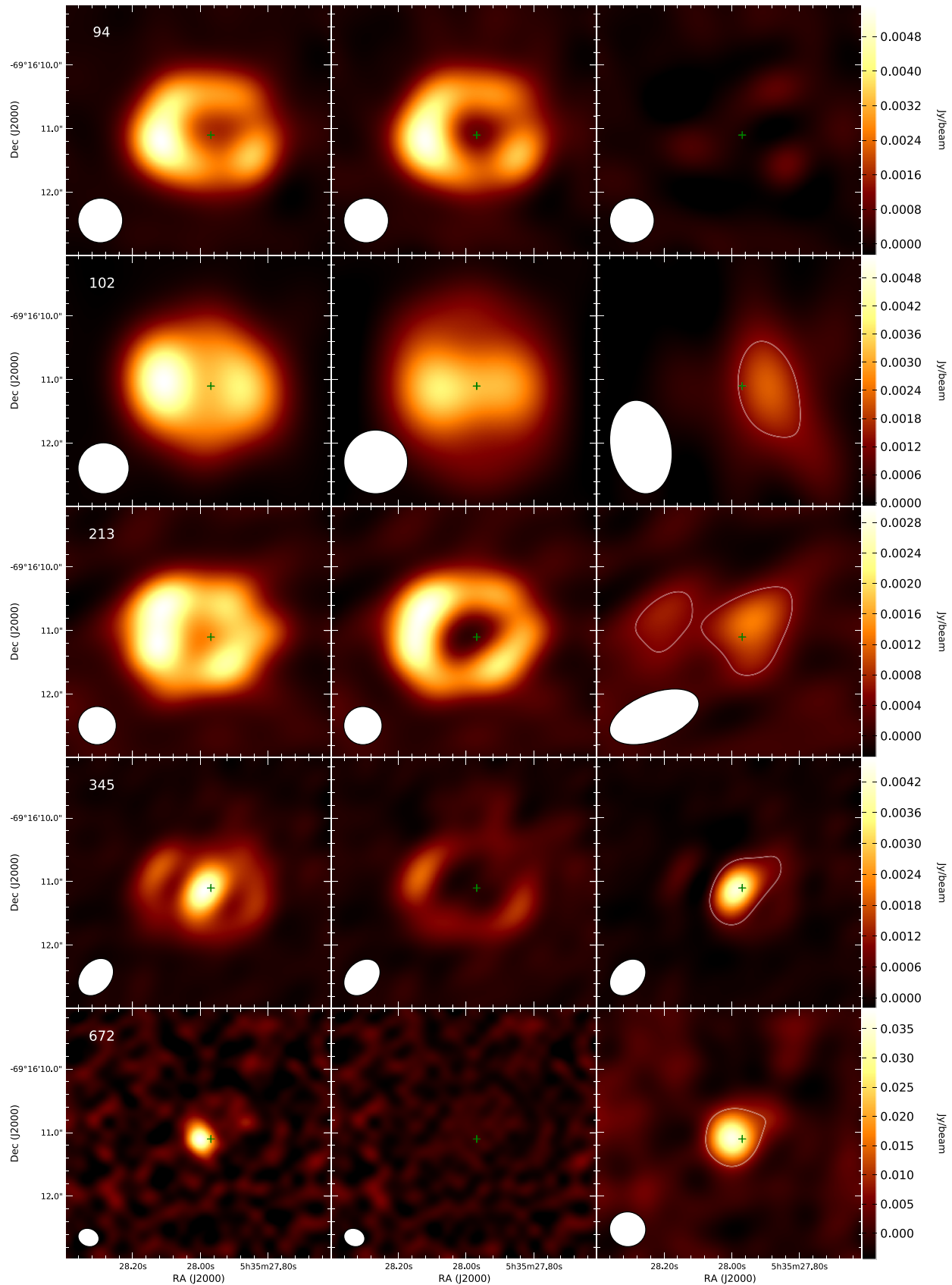[e] Images are shown in Figures 1 and 2.
[f] Images obtained by subtracting the model flux density at 672 GHz (I_{B9}) scaled to fit the central emission. See central column of Figures 1 and 2.
[g] Images obtained by subtracting the model flux density at 44 GHz (I_{44}) scaled to fit the toroidal emission. See left column of Figures 1 and 2.

imaged with ALMA at 672 GHz (B9; Indebetouw et al. 2014), were separately subtracted from the data sets at 94, 102, 213, 345, and 672 GHz. All subtractions were performed in the Fourier plane, via MIRIAD task uvmodel, where the model flux density at 44 GHz was scaled to fit the SNR emission over the ER (I_{44}), while the B9 model flux density was scaled to fit the emission localized in the central region of the remnant (I_{B9}). Scaling of the 44 GHz model was tuned by minimizing the flux density difference on the brighter eastern lobe, without over-subtracting in other regions of the remnant. To separate the emission in the SNR center, the central flux was firstly estimated by fitting a Gaussian model via MIRIAD task uvfit. The image model at 672 GHz was then scaled to match the flux of the Gaussian model. The scaling factor was further tuned to minimize over-subtraction.

Super-Nyquist sampling was applied in all images, using a pixel size of 8 mas to avoid artifacts when sources are not at pixel centers. Deconvolution via MEM was carried out on the residual images obtained from the subtraction of I_{B9}, while standard CLEANing was applied to the residuals obtained from the I_{44} subtraction. All diffraction-limited-subtracted images are shown in the central and right columns of Figure 1, while Figure 2 shows the residuals after super-resolution with the circular beam used for the original images. All image parameters are given in Table 2.

The flux densities were determined by integrating within polygons enclosing the SNR emission. Uncertainties in the flux densities include uncertainties in the image fitting/scaling process combined with the uncertainty in the flux density calibration. We note that the residual images from the subtraction

Figure 1. (Top to bottom) Left column: Stokes I continuum images of SNR 1987A at 94 (Lakićević et al. 2012b), 102, 213, 345, and 672 GHz. Images from 102 to 672 GHz are made from ALMA observations (Cycle 0) performed from 2012 April 5 to November 5 (see Table 1). Center column: images obtained by subtracting the model flux density at 672 GHz (Band 9) scaled to fit the central emission. Right column: images obtained by subtracting a scaled model flux density at 44 GHz (Zanardo et al. 2013), with 3σ flux density contours highlighted (white). The angular resolution is shown in the bottom left corner. The green cross indicates the VLBI position of SN 1987A as determined by Reynolds et al. (1995) [R.A. 05^h 35^m $27^s.968$, decl. $-69°$ $16'$ $11''.09$ (J2000)].

(A color version of this figure is available in the online journal.)
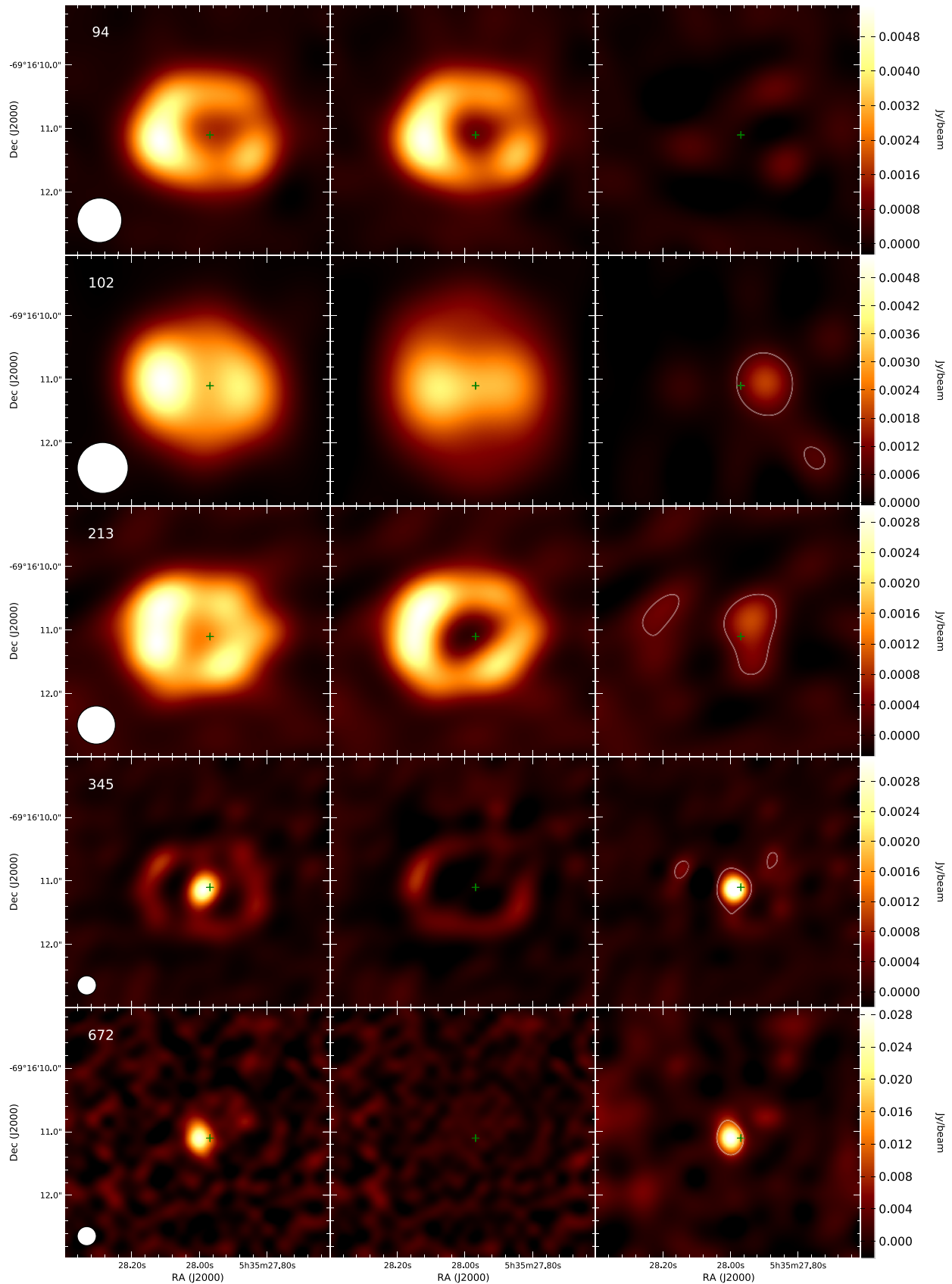
Figure 2. Panel layout is identical to that in Figure 1, but all Stokes *I* continuum-subtracted images are super-resolved. The circular beam used for the super-resolved ALMA images is 0″.8 at 102 GHz (Band 3), 0″.6 at 213 GHz (Band 6), 0″.3 at 345 (Band 7) and 672 GHz (Band 9), and is plotted in the lower left corner. The 94 GHz images are restored with a 0″.7 circular beam. For images in the right column, 3σ flux density contours are highlighted (white). The green cross indicates the VLBI position of SN 1987A as determined by Reynolds et al. (1995).

(A color version of this figure is available in the online journal.)
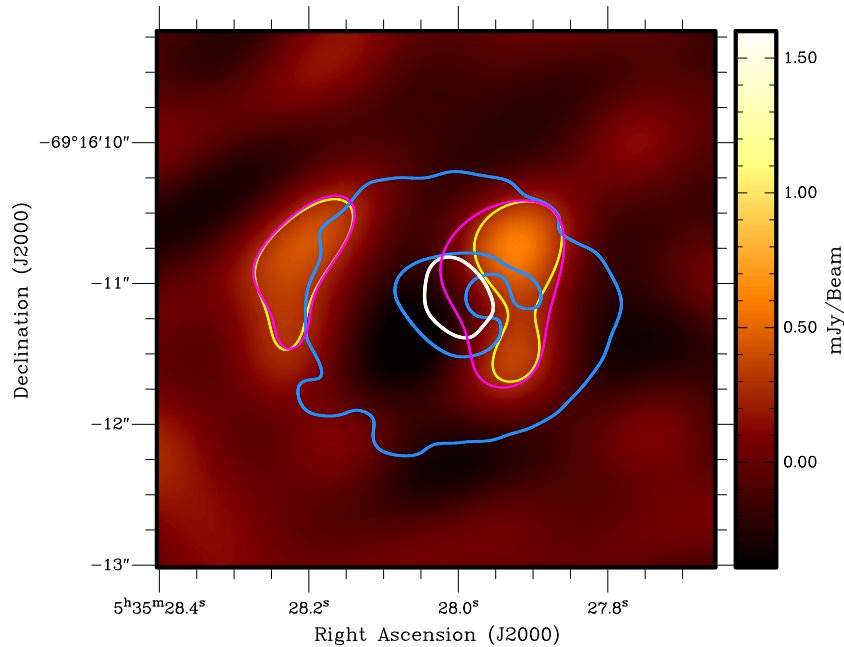
Figure 3. Stokes *I* continuum image of SNR 1987A at 213 GHz as obtained after the dual subtraction of the model flux densities at 44 and 672 GHz (see Section 2). The image is super-resolved with a 0″.6 circular beam, and the yellow contour highlights the 3σ flux density levels. The off-source rms noise is 0.14 mJy beam^{-1} (S/N ∼ 6σ). For comparison, the 213 GHz image obtained after the single subtraction of the model flux density at 44 GHz and similarly super-resolved with a 0″.6 circular beam (see Figure 2) is outlined via the 3σ flux density levels (magenta contours). The model images, i.e., the Stokes *I* images at 44 GHz (Zanardo et al. 2013) and at 672 GHz, are outlined by blue and white contours, respectively, at the 5σ flux density levels. Both model images are resolved with a 0″.3 circular beam.

(A color version of this figure is available in the online journal.)

of both models at 44 and 672 GHz were not considered, since the error attached to the double subtraction exceeds the total integrated flux density. Only at 213 GHz the error–flux margin is minor, as the diffraction-limited image obtained after the dual subtraction has integrated flux density of 2.1 ± 1.9 mJy (Figure 3).

3. MORPHOLOGY

ALMA observations of SNR 1987A capture both the remnant emission from the ER and that from the SNR interior, where the dense ejecta sit (Kamenetzky et al. 2013; Indebetouw et al. 2014).

While the image at 102 GHz barely resolves the two-lobe distribution of the emission, the images at 213 and 345 GHz clearly show the ringlike emission morphology, localized around the ER (see Figures 1 and 2). It is understood that the radio emission over the ER is primarily synchrotron emission, generated by the interaction of the SN shock with the dense CSM near the equatorial plane, which results in a magnetic-field discontinuity where particles are accelerated (e.g., Zanardo et al. 2010, 2013). As shown in early models of Type II SNRs (Chevalier 1982), the region of interaction between the SN blast and the CSM consists of a double-shock structure, with a forward shock, where ambient gas is compressed and heated, and a reverse shock, where the ejecta are decelerated. Between the two shocks, the reflected shocks, due to the forward shock colliding with the dense ER (Borkowski, Blondin & McCray 1997), propagate inward (Zhekov et al. 2009, 2010). The reverse shock at first expanded outward, behind the forward shock, but might have been inward-moving since day ∼7000. As discussed by Ng et al. (2013), the ring synchrotron emission is currently localized between the forward and reverse shocks, and likely has components from both the ER and high-latitude material above

the equatorial plane. Truncated-shell torus models of the remnant geometry at 9 GHz indicate that the half-opening angle has been decreasing since day ∼7000, and is estimated at ∼27° at day 9568 (Ng et al. 2013).

At 345 GHz the SNR interior is brighter, while at 672 GHz the emission is predominantly localized in the central region of the remnant. Since the emission from this region rises steeply with frequency, it has been identified with thermal dust emission (Indebetouw et al. 2014), as dust grains, probably heated by ^{44}Ti decay and X-ray emission from the reverse shock (Larsson et al. 2013), emit strongly in the FIR regime. The central emission, visible both in B7 and B9, appears to extend over the inner optical ejecta (see Figure 4). In particular, as noted by Indebetouw et al. (2014), this inner emission shows a north–south elongation, which in B9 can be identified between P.A. ∼ 20° and P.A. ∼ 30°, similar to that seen with *HST* (Larsson et al. 2011, 2013). From both Figures 1 and 2, it can also be noticed that the SNR emission at 672 GHz includes possible emission located to the NW (see contour overlays in Figure 5). This NW feature has signal-to-noise ratio (S/N) of 3.7σ, and integrated flux density of 6.8 ± 0.5 mJy, i.e., ∼10% of the total integrated flux density at 672 GHz.

3.1. Subtracted Images

To identify the origin of the emission in the I_{44}−subtracted images, with respect to the structure of the remnant as seen with *HST* (Larsson et al. 2011), the diffraction-limited residuals at 102, 213 and 345 GHz are superimposed in Figure 5. It can be seen that the residual at 102 GHz, characterized by $S/N|_{102} = 6.9σ$, is mainly located on the western lobe, west of the VLBI position of SN 1987A, as determined by Reynolds et al. (1995) [R.A. 05^h 35^m $27^s.968$, decl. $−69°$ $16'$ $11''.09$ (J2000)]. We note that, since the residual emission at 102 GHz has a constant flux per synthesized beam, the S/N is independent
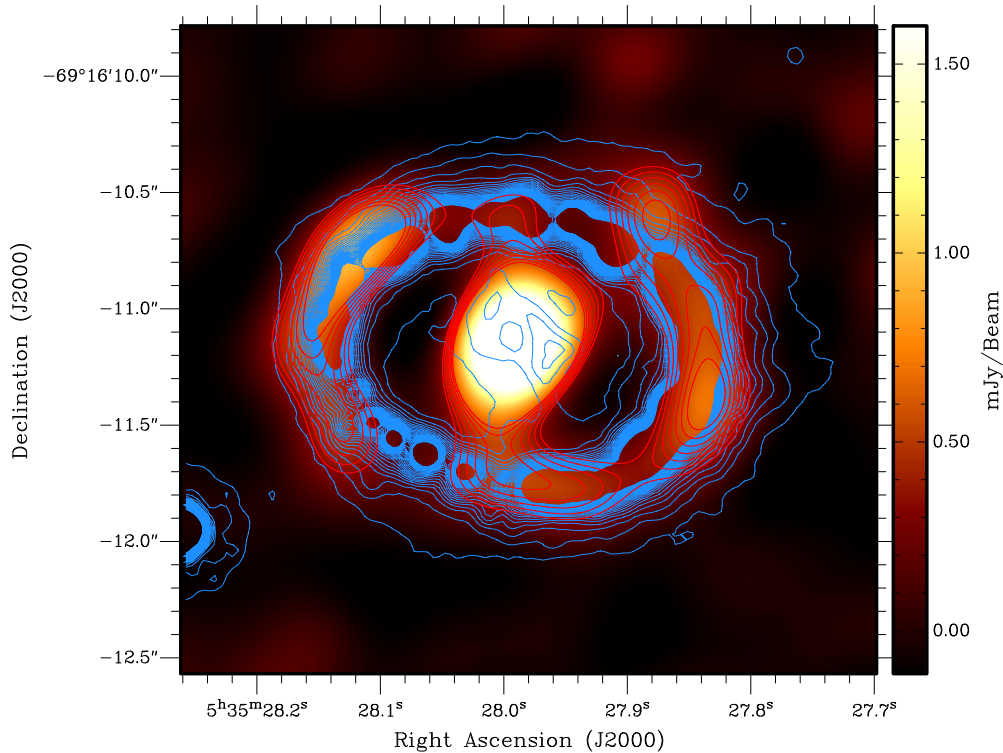
Figure 4. Overlay of the *HST* image of SNR 1987A (light blue contours; Larsson et al. 2011) on the 345 GHz image produced from ALMA observations performed in 2012 June and August (brown–yellow color scale and red contours). As in Figure 2, the ALMA image is super-resolved with a 0.″3 circular beam.

(A color version of this figure is available in the online journal.)

on the beam size. The emission at 213 GHz (orange contours in Figure 5), with $S/N|_{213} = 7.7\sigma$, peaks NW of the SN position, while fainter emission ($S/N|^{E}_{213} = 4.2\sigma$) may extend NE. The residual emission at both 102 and 213 GHz is above noise levels and, thus, unlikely to be the result of image artifacts. Given the brightening of the emission from the dust in the central region of the SNR, the residual images at 345 and 672 GHz have higher S/N. In particular, at 345 GHz (yellow contours in Figure 5) $S/N|_{345} = 17.4\sigma$, while, similar to the morphology at 213 GHz, the residual emission extends westward and elongates NW, with a much fainter spot on the north-eastern section of the ER ($S/N|^{E}_{345} = 2.4\sigma$). A westward-elongated morphology is present in the image at 672 GHz ($S/N|_{672} = 12.5\sigma$).

The I_{B9}−subtracted images emphasize the ring-like morphology of the synchrotron emission that mainly originates near the ER (see Section 3) and, thus, the asymmetry of this emission, which is discussed in Section 4. These residuals also highlight the presence of NW emission at 672 GHz, i.e., outside the inner SNR (see red contours in Figure 5). In fact, at 94, 213, and 345 GHz, it can be seen that the discontinuity in the NW sector of the ER, between P.A. $\sim 290°$ and P.A. $\sim 300°$, becomes more prominent after subtraction of the B9 model. Some extended emission north and NW of the ER emerges from noise at 345 GHz.

4. ASYMMETRY

The east–west asymmetry of the synchrotron emission, primarily associated with the emission morphology over the ER, is investigated from 44 to 345 GHz, as shown in Figure 6, where all images are restored with a 0.″7 circular beam. At 213 and

345 GHz the central dust emission is subtracted, via a scaled model of the flux density as resolved in B9 (see Section 2).

Considering radial sections crossing the SN site (Reynolds et al. 1995), the SNR asymmetry is first estimated as the ratio between the eastern peak of the radial slice crossing the maximum emission on the eastern lobe (see black/white profile in Figure 6), and the western peak of the radial slice crossing the maximum emission on the western lobe (see red profiles in Figure 6). This ratio, A_p, emphasizes the hot spots on each side of the remnant. Alternatively, the ratio A_i between the total flux densities integrated over the eastern and western halves of the image, is derived by splitting the image at the R.A. associated with the SN site. For comparison with previous asymmetry estimates (e.g., Zanardo et al. 2013), the ratio A_{90} between the eastern and western peaks of the radial slice at P.A. 90° (see dark green profile in Figure 6) is also derived. All values for A_p, A_i, and A_{90}, both for the images restored with a 0.″7 circular beam (as in Figure 6) and the diffraction-limited images, are plotted in Figure 7 and listed in Table 3.

From Figure 6 it can be seen that the A_{90} ratio does not fully capture the asymmetry changes with frequency, since the hot spot in the western lobe, which becomes brighter from 102 to 345 GHz, is located southward of the 90° profile. In Figure 7, the linear fits derived for both A_p and A_i ratios show a consistent decrease as frequencies reach the FIR. At 345 GHz, A_i values indicate that the east–west asymmetry is reversed, thus matching the asymmetry trend seen in recent *HST* images (Larsson et al. 2011), where the western side of the ring is markedly brighter. As discussed Section 3, the morphology similarities between the optical image of the SNR and the super-resolved image at 345 GHz are evident (see Figure 4).

The change of the remnant's east–west asymmetry over time has been discussed by Ng et al. (2013), as the result of
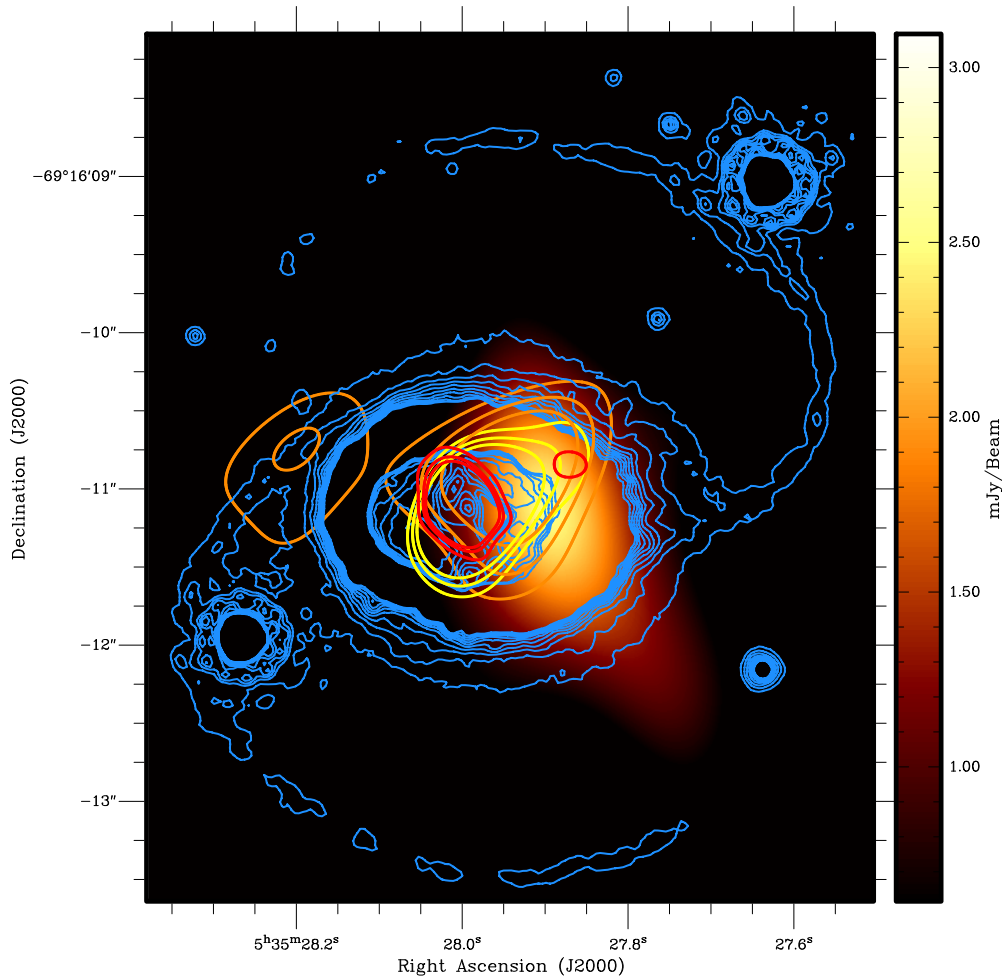
Figure 5. Comparison of the diffraction-limited images of SNR 1987A at 102, 213, and 345 GHz, as obtained after subtraction of the scaled model flux density at 44 GHz (see Figure 1, right column), with the optical image of the remnant. In detail, the residual image at 102 GHz (brown–yellow color scale) is overlaid with the contours outlining the residual images at 213 GHz (orange) and at 345 GHz (yellow). To locate the main sites associated with dust emission, the diffraction-limited image at 672 GHz is also outlined (red; as from Figure 1, left column). Images at 213, 345, and 672 GHz are overlaid with contours at 3σ, 4σ, and 5σ flux density levels. The angular beams associated with each image, as shown in Figure 1, are listed in Table 2. The *HST* image (Larsson et al. 2011) is outlined via contours (blue) that highlight the structure of the outer rings, the equatorial ring, and the ejecta.

(A color version of this figure is available in the online journal.)

a progressive flattening of the shock structure in the equatorial plane, due to the shock becoming engulfed in the dense UV–optical knots in the ER, coupled with faster shocks in the east side of the remnant. While X-ray observations do not show significant difference between the NE and SW reverse shock velocities, although the NE sector is brighter (Fransson et al. 2013), faster eastbound outer shocks have been measured in the radio (Zanardo et al. 2013) and point to an asymmetric explosion of a binary merger as SN progenitor (Morris & Podsiadlowski 2007, 2009). As the SN blast is gradually overtaking the ER, faster expanding shocks in the east would exit the ER earlier than in the west.

The effects of the asymmetric shock propagation are likely to emerge in the transition from radio to FIR rather than at lower frequencies, due to the shorter synchrotron lifetime at higher frequencies. To estimate the synchrotron lifetime in the FIR range, we use the approximation that, in a magnetic field of strength B, all the radiation of an electron of energy E is emitted only at the critical frequency ν_c (Rybicki & Lightman 1979). Considering the electrons orbit is inclined at a pitch angle θ to the magnetic field, the synchrotron lifetime, τ_e, can be derived

as a function of ν_c (e.g., Condon 1992)

$$\tau_e \equiv \frac{E}{|dE/dt|} \sim 1.06 \times 10^9 (B \sin\theta)^{-3/2} \nu_c^{-1/2}, \qquad (1)$$

where τ_e is expressed in years, B in μG, and ν in GHz. As the electrons are expected to have an isotropic distribution of pitch angles, $\langle \sin^2\theta \rangle = 2/3$; for $200 \lesssim \nu \lesssim 400$ GHz, and assuming a magnetic field strength at the shock front of $10 \lesssim B \lesssim 20$ mG (Berezhko & Ksenofontov 2006; Berezhko et al. 2011), in the radio/FIR transition we can estimate $20 \lesssim \tau_e \lesssim 80$ yr. However, since it is likely that sub-diffusive particle transport (Kirk et al. 1996) is taking place in regions of the SNR, in conjunction with efficient CR acceleration (Glushkov et al. 2013), local magnetic-field amplifications could exceed the above limits by at least an order of magnitude (Bell & Lucek 2001). In this scenario, the local τ_e would be of the order of months. Therefore, with regions in the remnant where electrons might be unable to cross the emission sites within their radiative life-time, the synchrotron emission at FIR frequencies would require the presence of relatively fresh injected and/or re-accelerated electrons to match the emission distribution at lower frequencies.
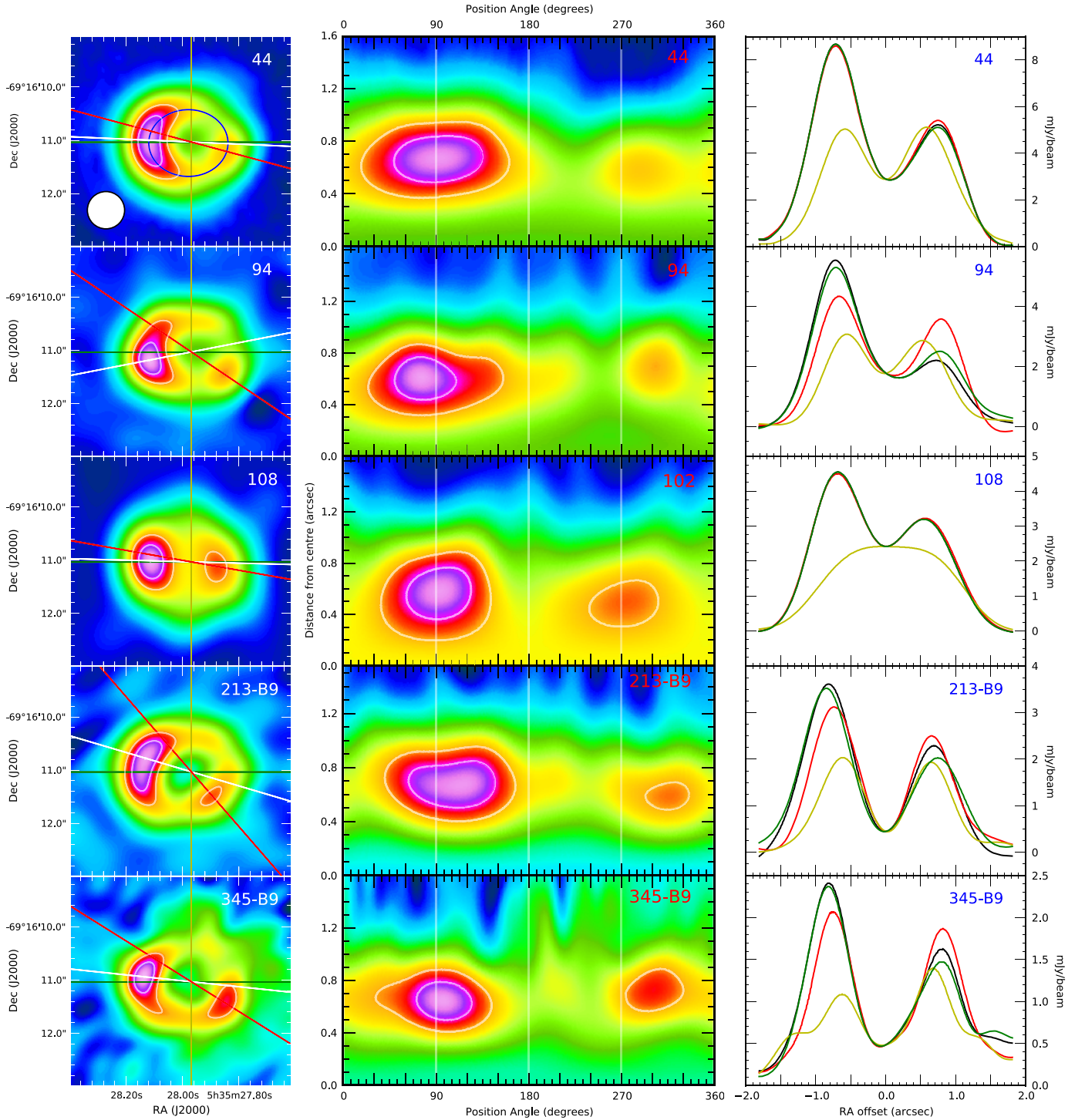
Figure 6. (Top to bottom) Left column: Stokes *I* continuum images of SNR 1987A at 44, 94, 102, 213, and 345 GHz. The 213 (213–B9) and 345 GHz (345–B9) images are derived after subtraction of the scaled model flux density at 672 GHz (Band 9, B9). All images are resolved with a 0".7 circular beam (as shown in the bottom left corner of the 44 GHz image). Center column: the images on the left column are converted to polar coordinates to visualize asymmetries in the two-dimensional radial distribution. The position angle and the projected radial distance from the geometrical center of the remnant are the new coordinates. Each image is projected along concentric ellipses (e.g., blue ellipse overlaid on the 44 GHz image). The emission intensity is conserved in the conversion. Contours at 65% and 85% levels of the emission are shown on all images (white). Right column: radial slices through each image at four position angles (as indicated on the images on the left column), which correspond to 0° (light green), 90° (dark green), emission peaks on the eastern lobe (white/black) and on the western lobe (red). The radial slices are plotted against the R.A. offset from the VLBI position of SN 1987A as determined by Reynolds et al. (1995) [R.A. 05^h 35^m 27^s.968, decl. −69° 16′ 11″.09 (J2000)].

(A color version of this figure is available in the online journal.)

5. SPECTRAL ENERGY DISTRIBUTION

The SED for ATCA data from 1.4 to 94 GHz and ALMA data is shown in Figure 8. To match the average epoch of the ALMA data, the ATCA data are scaled to day 9280, via exponential fitting parameters derived for ATCA flux densities from day 8000, as measured at 1.4, 8.6, and 9 GHz (G. Zanardo et al., in

Table 3
Asymmetry Ratios

Image	$A_p \equiv \dfrac{S_\nu(E_{Max})}{S_\nu(W_{Max})}$ [a]		$A_i \equiv \int_E S_\nu / \int_W S_\nu$ [b]		$A_{90} \equiv S_\nu\left(\dfrac{E_{Max}}{W_{Max}}\right)\Big|_{90°}$ [c]	
GHz	0″.7 [d]	DL [e]	0″.7	DL	0″.7	DL
44	1.61 ± 0.08	1.42 ± 0.05	1.36 ± 0.02	1.53 ± 0.07	1.69 ± 0.08	1.54 ± 0.05
94	1.55 ± 0.05	⋯	1.18 ± 0.04	⋯	1.88 ± 0.07	⋯
102	1.44 ± 0.04	⋯	1.10 ± 0.04	⋯	1.40 ± 0.07	⋯
213	1.28 ± 0.03	1.43 ± 0.05	1.24 ± 0.06	1.23 ± 0.02	1.43 ± 0.02	1.49 ± 0.05
$213 - I_{B9}$ [f]	1.44 ± 0.03	⋯	1.30 ± 0.02	⋯	1.19 ± 0.03	⋯
345	⋯	1.28 ± 0.03	⋯	0.78 ± 0.04	⋯	1.16 ± 0.03
$345 - I_{B9}$ [f]	1.30 ± 0.02	⋯	0.80 ± 0.02	⋯	1.48 ± 0.04	⋯

Notes.
[a] Ratio between the eastern peak of the radial slice crossing the maximum emission on the eastern lobe, and the western peak of the radial slice crossing the maximum emission on the western lobe (see black/white and red profiles in Figure 6).
[b] Ratio between the total flux densities integrated over the eastern and western halves of the image. The image is split at the R.A. associated with the SN site (Reynolds et al. 1995).
[c] Ratio between the eastern and western peaks of the radial slice at P.A. 90° (see dark green profile in Figure 6).
[d] Images resolved with a 0″.7 circular beam (see Figure 6).
[e] Diffraction-limited (DL) images (see Figure 1).
[f] Images derived after subtraction of the model flux density at 672 GHz (Band 9, B9), scaled to fit the central emission (see Figure 6).
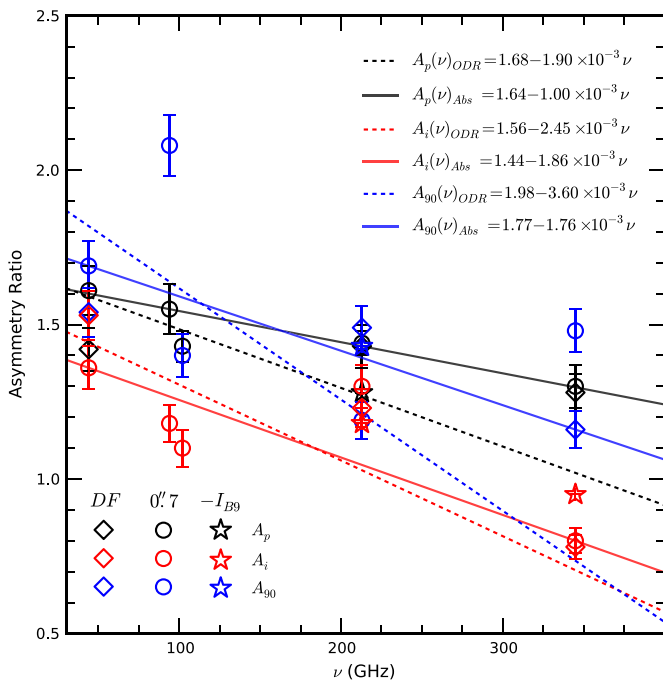
Figure 7. Asymmetry ratios of Stokes I images of SNR 1987A from 44 to 345 GHz. With reference to Table 3, the east–west asymmetry ratios estimated via three different methods are indicated as: A_p (black symbols); A_i (red symbols); A_{90} (blue symbols). Asymmetry ratios are derived from the diffraction-limited images (diamonds; see Figure 1), from the images restored with a 0″.7 circular beam (circles; see Figure 6), and from images obtained after the subtraction of the dust emission component (stars; see Figure 6). Tentative linear fits are shown for A_p (black fits), A_i (red fits), and A_{90} (blue fits), based on all ratios derived via each method. The orthogonal distance regression (A_{ODR}) and the robust fitting from the square root of absolute residuals (A_{Abs}) are tested for linear interpolation. The combined fits for the A_p and A_i ratios yield an average $A(\nu) \sim A(\nu_0) - 1.9 \pm 0.8 \times 10^{-3}\nu$, where ν is expressed in GHz and $A(\nu_0 = 30) = 1.57 \pm 0.13$.
(A color version of this figure is available in the online journal.)

preparation; Staveley-Smith et al. 2014). Across the transition from radio to FIR frequencies, the observed spectrum consists of the sum of thermal and non-thermal components.

As described in Section 2, to identify the dust component of the emission from the inner regions of the remnant, the B9 model flux density, S_{B9}, has been scaled to fit the emission measured in the SNR central region at 94–345 GHz ($S_{B9\,fit}$, hollow red circles in Figure 8). The subtraction of $S_{B9\,fit}$ from the visibilities at 94–345 GHz yields the residual flux densities indicated as $S_\nu - S_{B9\,fit}$ (purple bars in Figure 8), as for the images shown in the central column of Figure 1. The flux densities $S_{B9\,fit}$ derived in B6 and B7, together with the total integrated flux density measured in B9 (S_{B9}), although obtained via a different reduction technique, have been associated by Indebetouw et al. (2014) with dust grains, in conjunction with data from *Herschel* (Matsuura et al. 2011) and the Atacama Pathfinder Experiment (APEX; Lakićević et al. 2012a; Figure 8).

Similarly (see Section 2), to separate the non-thermal emission from that thermal, the 44 GHz model flux density, S_{44}, has been scaled to fit the toroidal component of the emission at 94–672 GHz (blue/cyan diamonds in Figure 8). By fitting the resulting $S_{44\,fit}$ components and the ATCA flux densities at 1.4–44 GHz, we obtain, at day 9280, the synchrotron spectral index $\alpha_s = -0.727 \pm 0.020$, with $S_\nu(\alpha_s) \propto \nu^{\alpha_s}$. The spectral index measured from 1.4 to 94 GHz, i.e., for ATCA data only, is $\alpha_{ATCA} = -0.735 \pm 0.028$. While α_s is slightly flatter than α_{ATCA}, both values are consistent with the progressive flattening of the radio spectrum measured since day ∼5000 (Zanardo et al. 2010). The subtraction of $S_{44\,fit}$ from the visibilities at 94–672 GHz, gives the residual flux densities $S_\nu - S_{44\,fit}$ (red/orange diamonds in Figure 8), as for the images shown in the right column of Figure 1. In B3, B6, and B7, $S_\nu - S_{44\,fit} > S_{B9\,fit}$, i.e., the residuals exceed the emission expected from the dust.

While the subtraction of the flux densities is inevitably affected by errors (see Table 2), given that the I_{44}−subtracted images have a S/N $\gtrsim 7\sigma$ and the residual emission appears primarily located westward of the optical ejecta (see Section 3.1), we investigate the nature of this emission excess as: (1) free–free emission from an ionized fraction of the inner ejecta, (2) synchrotron emission from a compact source located in the inner regions of the remnant, and (3) emission from grains of very cold dust.
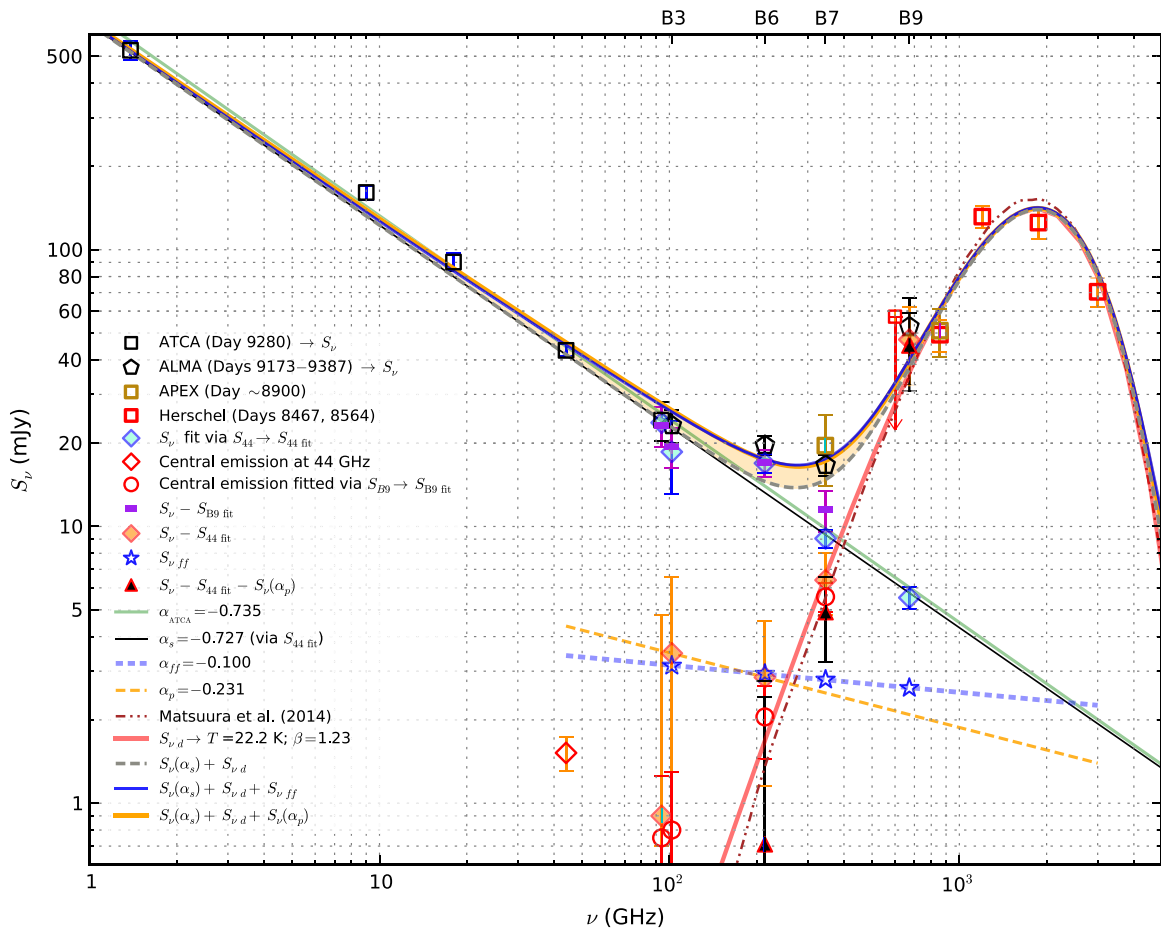
Figure 8. Spectral energy distribution (SED) of SNR 1987A from radio to FIR, with data from: ATCA at 1.4 GHz (G. Zanardo et al., in preparation), 9 GHz (Ng et al. 2013), and 18 and 44 GHz (Zanardo et al. 2013), and 94 GHz (Lakićević et al. 2012b); ALMA at 102 GHz (Band 3, B3), 213 GHz (Band 6, B6), 345 GHz (Band 7, B7), and 672 GHz (Band 9, B9; this paper); the Atacama Pathfinder EXperiment (APEX) at 345 and 857 GHz (Lakićević et al. 2012a); the *Herschel Space Observatory* at 600–3000 GHz (Matsuura et al. 2011). The brown dash-dot-dotted curve is the amorphous carbon dust fit for ALMA data and *Herschel* observations carried out in 2012 (Matsuura et al. 2014). To match the average epoch of ALMA observations, ATCA data are scaled to day 9280, via exponential fitting parameters derived for ATCA flux densities from day 8000, as measured at 1.4, 8.6, and 9 GHz (G. Zanardo et al., in preparation; Staveley-Smith et al. 2014). The hollow red diamond indicates the central emission measured at 44 GHz as reported by Zanardo et al. (2013), scaled to day 9280. The difference between possible spectral fits is highlighted in light orange. See Section 5 for a detailed description of this figure.

(A color version of this figure is available in the online journal.)

5.1. Free–Free Emission

To estimate the free–free radiation in the SNR as imaged with ALMA, we hypothesize an ionized portion of the ejecta as an approximately spherical region, located inside the ER. Using the beam size of the super-resolved I_{44}−subtracted image at 102 GHz as an upper limit, we consider the radius of the spherical region up to $R_s \sim 0\rlap{.}''40$ ($\approx 3.08 \times 10^{17}$ cm). Such radius covers the extent of the inner ejecta as imaged in the optical (Larsson et al. 2013), and stretches to the likely radius of the reverse shock, qualitatively identified with the inner edge of the emission over the ER (see Figure 4). Given that the pre-SN mass has been estimated between $14\,M_\odot$ and $20\,M_\odot$ (Smartt 2009), if we assume that the HII region in the ejecta has a uniform density $\rho_{ej}(r) = 3\,M_{\mathrm{HII}}(4\pi r^3)^{-1}$, we set $0.7\,M_\odot \lesssim M_{\mathrm{HII}} \lesssim 2.5\,M_\odot$. The lower limit, $M_{\mathrm{HII}} \sim 0.7\,M_\odot$, i.e., $\rho_{ej}(r = R_s) = 1.1 \times 10^{-20}$, represents a partial ionization of the ejecta by X-ray flux, either within the inner region or on the outer layer. The upper limit, $M_{\mathrm{HII}} \sim 2.5\,M_\odot$, i.e., $\rho_{ej}(r = R_s) = 4.1 \times 10^{-20}$ g cm^{-3} matches the density model by Blinnikov et al. (2000) scaled to the current epoch (see Figure 21 in Fransson et al. 2013), and corresponds to complete ionization of the H and He mass within R_s.

The optical depth associated with the HII region along the line of sight (los) can be estimated as

$$\tau_{\mathrm{ff}} \approx 3.28 \times 10^{-7}\, T_4^{-1.35}\, \nu^{-2.1}\, N_e^2 R_s, \qquad (2)$$

where $T_4 = T_e/(10^4\,\mathrm{K})$, ν is in GHz, N_e is in cm^{-3} and $R_s \approx \int_{\mathrm{los}} dl$ is in pc. For $T_4 \sim 1$, given the emission measure $4.6 \times 10^6 \lesssim \mathrm{EM} \lesssim 5.9 \times 10^7$ cm^{-6} pc, where $\mathrm{EM} = N_e^2 R_s$, at frequencies $102 \lesssim \nu \lesssim 672$ GHz the emission becomes nearly transparent as $2.28 \times 10^{-6} \lesssim \tau_{\mathrm{ff}} \lesssim 1.2 \times 10^{-3}$. The flux associated with the ionized component of the ejecta, can then be derived as

$$S_{\nu_{\mathrm{ff}}} \propto \tau_{\mathrm{ff}}(\nu)\frac{2kT}{\lambda^2}\Omega \propto \nu^{-0.1}. \qquad (3)$$

Considering the solid angle Ω subtended by the same radius, R_s, at all frequencies, for the lower limit $M_{\mathrm{HII}} \approx 0.7\,M_\odot$, i.e., $N_e = 6.8 \times 10^3$ cm^{-3}, $S_{\nu_{\mathrm{ff}}} \sim (S_\nu - S_{44\,\mathrm{fit}})$ at 102 and 213 GHz, as Equation (3) yields $S_{102_{\mathrm{ff}}} \sim 3.9$ mJy, $S_{213_{\mathrm{ff}}} \sim 3.2$ mJy, $S_{345_{\mathrm{ff}}} \sim 3.1$ mJy, and $S_{672_{\mathrm{ff}}} \sim 2.9$ mJy. These $S_{\nu_{\mathrm{ff}}}$ values (blue stars in in Figure 8) would well fit the SED (see blue fit in Figure 8). If the HII density is considerably higher, as given by

the upper limit $M_{\mathrm{H\,II}} \approx 2.5\,M_\odot$, the derived $S_{\nu_{\mathrm{ff}}}$ fluxes would exceed the emission residuals by an order of magnitude.

As a constraint to the free–free emission component, the hypothesized H II region would also produce optical and near-IR H I recombination lines. The resultant Hα flux can be estimated as

$$S_{\mathrm{H}\alpha} \approx \epsilon\, N_e N_+ \left(\frac{4}{3}\pi R_s^3\right)\frac{f}{4\pi d^2}, \tag{4}$$

where $\epsilon \propto \alpha_A$ is the emissivity of the Hα line per unit volume, with $\alpha_A = \alpha_A(T) = \sum_n \alpha_n(T)$ the total recombination coefficient, f is the volume filling factor and d is the distance to the source. If one adopts $\epsilon \approx 3.53 \times 10^{-25}\, T_4^{-0.92}$ erg cm^{-3} s^{-1} for $T_4 \simeq 0.5$ (e.g., Storey & Hummer 1995), the number of ions $N_+ = N_e = 6.8 \times 10^3$ cm^{-3} as for the lower limit assumed for the density of the H II region, and $R_s \approx 3.08 \times 10^{17}$ cm, for $f \sim 1$ one obtains $S_{\mathrm{H}\alpha} \approx 1.26 \times 10^{-11}$ erg cm^2 s^{-1}. To match the Hα flux from the core measured by Fransson et al. (2013) (see Figure 8 therein) at $\sim 1.4 \times 10^{-14}$ erg cm^2 s^{-1} on day 9000, the estimated $S_{\mathrm{H}\alpha}$ would have to undergo 7.4 mags of extinction. Such extinction is possible but improbable. We note that the above $S_{\mathrm{H}\alpha}$ also exceeds the Hα emission by the reverse shock, measured at $\sim 2.0 \times 10^{-13}$ erg cm^2 s^{-1} on day 9000, and associated with a density $250 \lesssim N_+ \lesssim 750$ cm^{-3} (Fransson et al. 2013).

As regards the magnitude of the flux from the Br-γ line, the model estimate by Kjær et al. (2010) on day 6840 is a factor of $\sim 10^{-2}$ smaller than the $S_{\mathrm{H}\alpha}$ derived from Equation (4), while this is mainly associated with emission from the hot spots in the ER.

In the absence of external X-ray heating, both the heating and ionization would be powered by radioactive decays in the core. The resultant flux, estimated via models as in Kozma & Fransson (1998), would be several orders of magnitude smaller than the lower limit for $S_{\nu_{\mathrm{ff}}}$.

Another possible source of ionizing emission is a pulsar wind nebula (PWN) in the SNR interior. The properties of any PWN are very uncertain (see Section 7), but there is the expectation that line emission would accompany free–free emission also in this case.

5.2. Flat-spectrum Synchrotron Emission

A flat spectral index could also be attributed to a second synchrotron component. As shown in Figure 8, within $102 \leqslant \nu \leqslant 672$ GHz, a synchrotron component with spectral index $\alpha_p = -0.231$ fits the residuals ($S_\nu - S_{44\,\mathrm{fit}}$) at 102 and 213 GHz. Synchrotron emission with $-0.4 \lesssim \alpha \lesssim -0.1$ fits the spectrum in the radio/FIR transition and could originate from a compact source near the center of the SNR. In the case of a central pulsar, the synchrotron emission would be generated by the shocked magnetized particle wind (Gaensler & Slane 2006). The scenario of a synchrotron-emitting PWN in the inner SNR is explored in Section 7.

5.3. Dust Emission

If the excess emission is due to an additional synchrotron component, $S_\nu(\alpha_p) \propto \nu^{-0.2}$, this would provide a constraint to the net dust emission, S_{ν_d}, in ALMA data. The subtraction $S_\nu - S_{44\,\mathrm{fit}} - S_\nu(\alpha_p)$, where $S_{\nu_p} = S_{0_p}(\nu/\nu_0)^{\alpha_p}$ with $S_{0_p} = 3.5 \pm 3.1$ mJy as from Table 2, leads to $S_{213_d} \sim 0.7$ mJy, $S_{345_d} \sim 4.9$ mJy and $S_{672_d} \sim 45.0$ mJy (black triangles in Figure 8). We note that S_{672_d} coincides with the integrated flux

density of the central feature of the related image, which extends over the inner ejecta as seen with *HST* (see Figure 4). The net dust can be fitted via a modified Planck curve of thermal emission, as

$$S_{\nu_d}(\beta, T) = \frac{M_{\mathrm{dust}}}{d^2}\,\kappa_\nu\, B_\nu(T) \propto \nu^\beta\, B_\nu(T), \tag{5}$$

where M_{dust} is the dust mass, $\kappa_\nu = 3\,Q_\nu/4\rho\,a_\nu$ is the dust mass absorption coefficient, with Q_ν the absorption efficiency for spherical grains of density ρ and radius a_ν, $1 \lesssim \beta \lesssim 2$ for insterstellar dust (e.g., Cortese et al. 2014 and references therein) and $B_\nu(T)$ is the Planck function. As shown in Figure 8, the best fit of both ALMA fluxes, as reported in this paper, and *Herschel* fluxes, as from Matsuura et al. (2011), yields $\beta = 1.23$ and dust temperature $T = 22.2$ K. The thermal peak of the SED has been previously fitted (Matsuura et al. 2011; Lakićević et al. 2011, 2012b, 2012a) with temperatures estimated between 17 and 26 K, while Indebetouw et al. (2014) fit amorphous carbon dust at $T = 26 \pm 3$ K.

The sum of the main synchrotron component, $S_\nu \propto \nu^{-0.73}$, and the emission component from dust grains at $T \sim 22$ K is lower than the measured ALMA flux densities at 213 and 345 GHz (see dashed gray fit in Figure 8). To match the emission excess of ~ 3 mJy in this frequency range, we could also postulate a second dust component. This would require very cold dust at $T \lesssim 5$ K, i.e., at temperatures where the assumption of either amorphous carbon or silicates leads to dust masses implausibly large for physically realistic grains. In particular, as from Equation (5), at 345 GHz a flux density of ~ 3 mJy would require dust at $T \sim 3$ K with $M_{\mathrm{dust}} \sim 50\,M_\odot$, as obtained by using $k_\nu \sim 2.5$ cm^2 g^{-1} for amorphous carbon (Zubko et al. 1996, 2004). We note that warmer dust at $T \sim 180$ K has been identified by Dwek E. et al. (2010) in the ER, where the dust grains are likely collisionally heated by the expanding radiative shocks (Bouchet et al. 2006).

6. SPECTRAL INDEX VARIATIONS

The spectral index distribution across the remnant is investigated via multi-frequency spectral index maps and the T–T plot method (Costain 1960; Turtle et al. 1962).

Spectral index maps are derived from images at 44, 94, 102, 213, and 345 GHz. In Figure 9, the maps resulting from the combination of images at two, three, four and five frequencies are shown. All images are reduced with identical procedure and restored with a circular beam of 0′′.8. ATCA data at 44 and 94 GHz are scaled to day 9280, via exponential fitting parameters derived for ATCA flux densities from day 8000, as measured at 8.6 and 9 GHz (G. Zanardo et al., in preparation). While the two-frequency maps are derived from direct division of the flux densities, the maps derived from three to five frequencies are more accurate, as the solution minimizes the function

$$\boldsymbol{\varepsilon}_{pq} = \sum_{k=1}^{n} \left| S_{\nu_k}^{pq}\left(\alpha_M^{pq}\right) - S_{\nu_0}^{pq}\left(\frac{\nu_k}{\nu_0}\right)^{\alpha_M^{pq}} \right|^2 \tag{6}$$

at each pixel of coordinates (p, q), for images at ν_k frequencies, with $n \geqslant 3$.

In Figure 9, it can be seen that the spectral indices overall become flatter as the frequencies reach the FIR. For all maps, the spectral index, α_M, varies between -1.25 and 0.25, while in the five−frequency map the index range narrows to $-0.96 \leqslant \alpha_M \leqslant 0.18$. In most of the multi-frequency maps, α_M is steeper on the
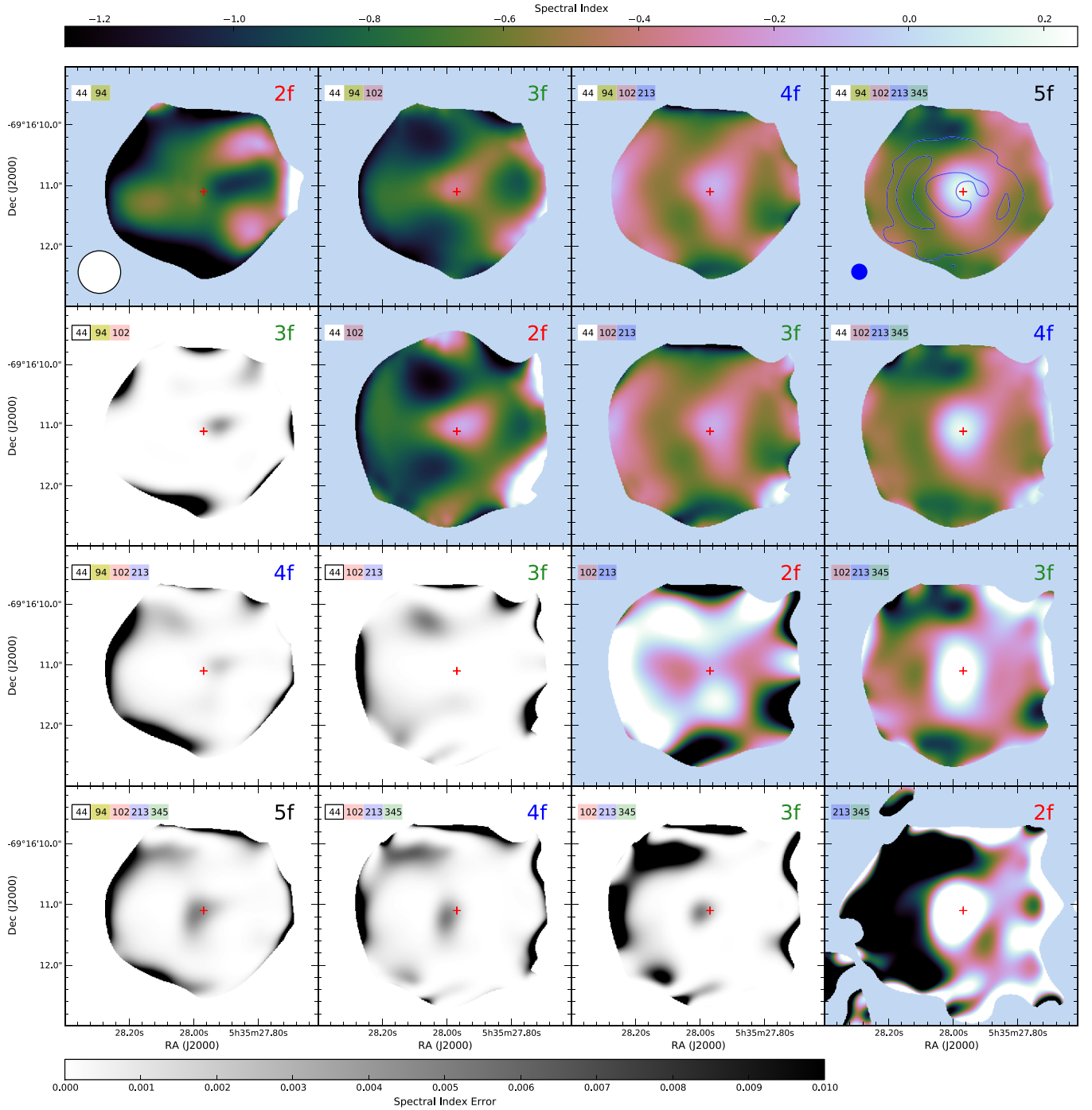
Figure 9. In color scale are maps of the spectral index distribution in SNR 1987A, as derived from images at 44, 94, 102, 213, and 345 GHz. The source images are reduced with identical procedure and restored with a circular beam of 0''.8. To match the average epoch of ALMA observations, ATCA data at 44 and 94 GHz are scaled to day 9280, via exponential fitting parameters derived for ATCA flux densities from day 8000, as measured at 8.6 and 9 GHz (G. Zanardo et al., in preparation). The spectral maps are derived from flux densities at 2, 3, 4, and 5 frequencies, and labeled as *2f*, *3f*, *4f*, and *5f*, respectively (top right corner). The frequencies used in each map are indicated, in GHz, on the top left corner. Image regions below the highest rms noise level are masked. The upper limit of the spectral index color scale is set to $\alpha = 0.25$; therefore, map regions with spectral indices greater than 0.25 appear in white. In gray scale are maps of the error associated with α in the power-law fit, $S_\nu \sim \nu^\alpha$, used for spectral maps of flux densities at 3, 4, and 5 different frequencies, and labeled as *3f*, *4f*, and *5f*, respectively. To emphasize the error distribution, while using a linear gradient of the gray color scale, map regions with errors greater than 0.01 appear in black. In the top right map, the contours of the 44 GHz image, resolved with a 0''.25 circular beam, are shown at the 15% and 60% emission levels (in blue). The red cross indicates the VLBI position of SN 1987A as determined by Reynolds et al. (1995) [R.A. 05^h 35^m 27^s.968, decl. −69° 16' 11''.09 (J2000)].

(A color version of this figure is available in the online journal.)

eastern half of the SNR, while flat spectral indices surround the center, where the bulk of dust sits (see Section 3), and extend onto the NW and SW regions of the remnant. With reference to the five-frequency map, $-0.9 \lesssim \alpha_M \lesssim -0.6$ on the eastern lobe and $-0.4 \lesssim \alpha_M \lesssim 0$ on the western side of the SNR, with $\alpha_M \sim 0$ around the central region and $-0.4 \lesssim \alpha_M \lesssim -0.3$ predominantly in the NW quadrant (P.A. $\sim 330°$) and in the SW quadrant (P.A. $\sim 210°$).
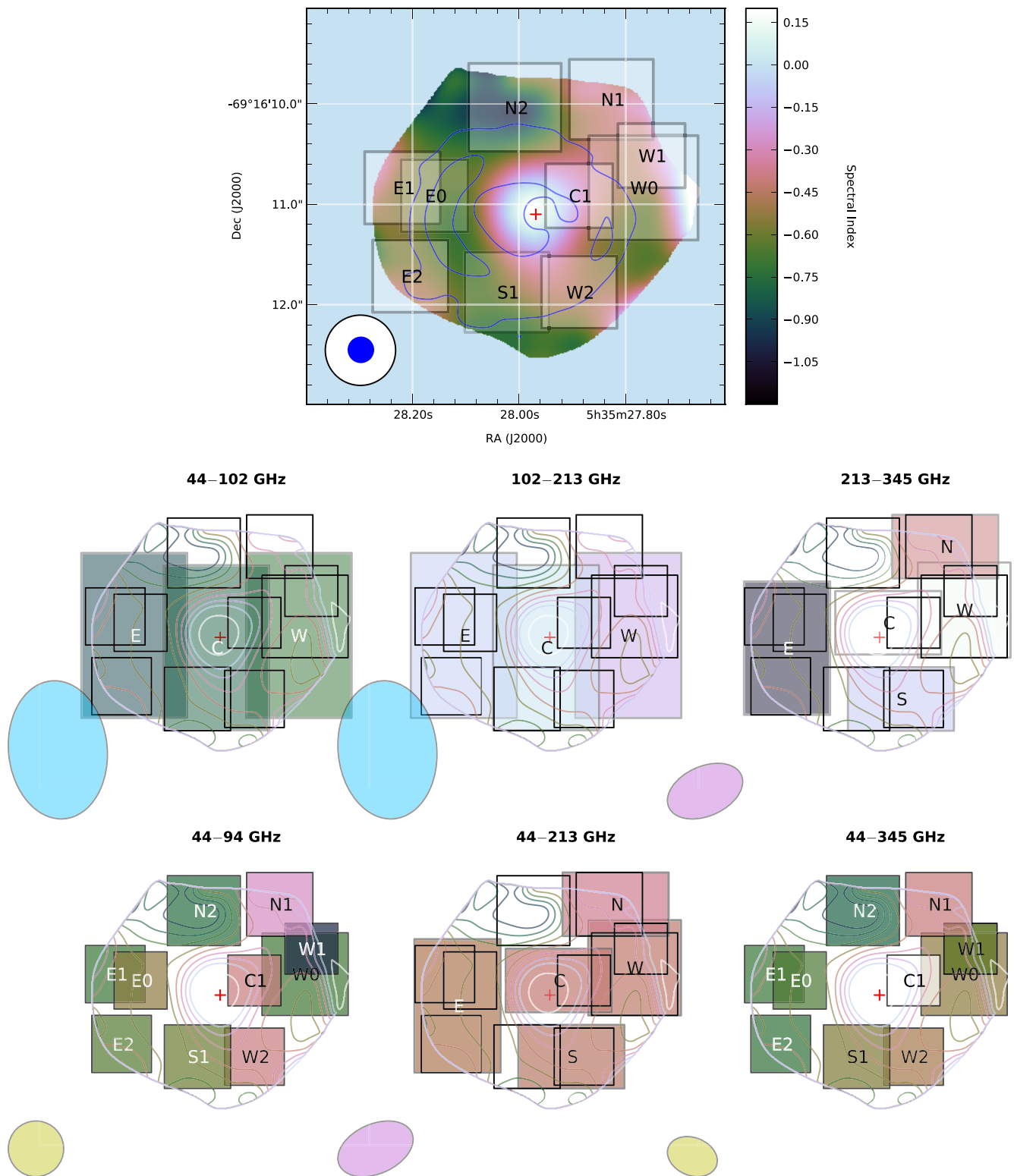
Figure 10. Top: four-frequency (44–94–213–345 GHz) spectral index intensity map with an angular resolution of 0''8, where ATCA data at 44 and 94 GHz are scaled to day 9280. The map is superimposed with the contours of the 44 GHz image, resolved with a 0''25 circular beam, at the 15% and 60% emission levels (in blue). The regions used to derive the spectral indices $\alpha_{\rm TT}$, via T–T plots, are indicated by gray/white squares. Bottom: the T–T plots are applied to six pairs of frequencies: 44–102 GHz, 102–213 GHz, 213–345 GHz, 44–94 GHz, 44–213 GHz, and 44–345 GHz. The controlling beam associated with each pair of frequencies is shown on the lower left corner of the images. The T–T boxes are color-coded according to the resultant $\alpha_{\rm TT}$ value. For image pairs of angular resolution lower than 0''8, larger T–T boxes are used as outlined. All T–T boxes are drawn on top of the four-frequency spectral map, highlighted by contours spaced at $\Delta\alpha = 0.1$, which are colored according to the associated spectral index. The red cross indicates the VLBI position of SN 1987A as determined by Reynolds et al. (1995). The $\alpha_{\rm TT}$ values resulting from the six frequency pairs are detailed in Table 4.

(A color version of this figure is available in the online journal.)
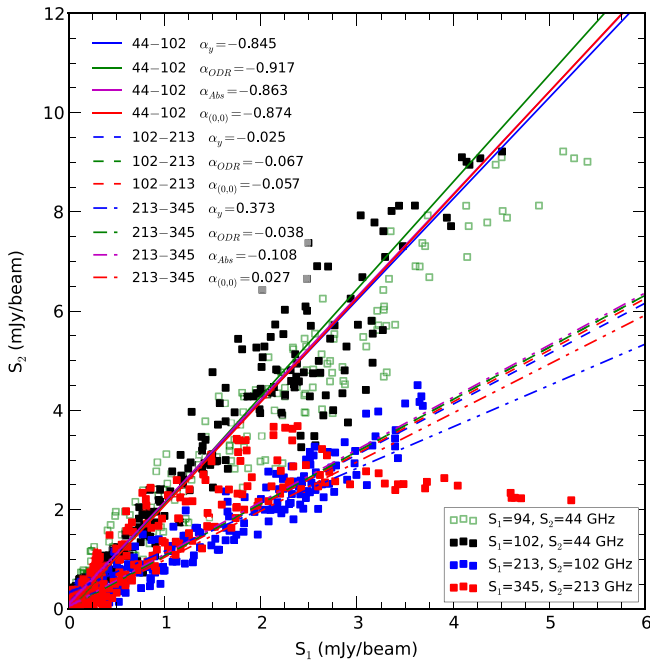
Figure 11. T–T plot of the whole SNR, where flux densities (S_1 vs. S_2) are plotted instead of brightness temperatures. Four frequency pairs are included: 44–94 GHz (green hollow squares); 44–102 GHz (solid black squares); 102–213 GHz (solid blue squares); 213–314 GHz (solid red squares). Data points for the 44–94 GHz frequency pair are not fitted. The given spectral indices are derived from different linear interpolations: least-square fit from vertical squared errors, α_y (blue); orthogonal distance regression, α_{ODR} (green); robust fitting from the square root of absolute residuals, α_{Abs} (magenta); linear regression with forced zero interception ($S_1 = 0$, $S_2 = 0$), $\alpha_{(0,0)}$ (red).

(A color version of this figure is available in the online journal.)

The T–T plot method is applied to two images at different frequencies, each obtained with identical reduction process and with the same angular resolution. The spectral variations are assessed over image regions not smaller than the beam size, where the spectral index, α_{TT}, is determined from the flux density slope m, where $S_2 = m\,S_1 + q$. The regions used for the T–T plots are shown in Figure 10. Six frequency pairs are considered: $44-102$ GHz, $102-213$ GHz, and $213-345$ GHz; and $44-94$ GHz, $44-213$ GHz, and $44-345$ GHz. Different box sizes are used to suit the controlling beam of each frequency pair. All derived α_{TT} values are listed in Table 4.

Similarly to the trend of α_M, α_{TT} values become flatter at higher frequencies (see Figure 11). From 102 to 213 GHz, $\alpha_{TT} \approx -0.1$ across the whole remnant (see Figure 10), while from 213 to 345 GHz the spectral distribution appears markedly split in two larger regions (see also the two-frequency map in Figure 9), with very flat indices on the western half of the SNR and steep indices on the eastern side. For the frequency pairs 102–213 and 213–345 GHz, the T–T plots for the eastern region (see E in Table 4) give $\Delta\alpha_{TT} = \alpha_{(102,\,213)} - \alpha_{(213,\,345)} = 1.0 \pm 0.07$. This could be indication of a local spectral break at 213 GHz. Using $\nu_c = 213$ GHz in Equation (1), for $B = 20$ mG, $\tau_e \sim 35$ yr. However, given the high Mach number ($\mathcal{M} \sim 10^4$) of the eastbound shocks (Zanardo et al. 2013), likely sub-diffusive particle transport (Kirk et al. 1996) by the shock front and, consequently, local magnetic-field amplifications (Bell 2004), it is possible that the CR in the eastern lobe, radiating at ν_c, are already past their synchrotron lifetime.

Flat spectral indices in the western lobe extend north and south at both 213–345 GHz and 44–213 GHz (see Figure 10), while T–T plots from higher resolution images show a narrower north–south alignment of the flat regions (see N1, C1 and W2 in Figure 10 and Table 4), with $-0.5 \lesssim \alpha_{TT} \lesssim -0.3$. The T–T plots for 44–94 GHz and 44–345 GHz also yield the steepest spectral indices in region W1, this might be due to the local emission drop in the NW sector of the ER, visible in the images at 94 and 345 GHz at P.A. $\sim 300°$.

As discussed in Section 5, the flat-spectrum western regions could be linked to a PWN. We note that spectral maps of the Crab Nebula via observations centered at 150 GHz (Arendt et al. 2011) have identified spectral indices around -0.2 in the inner central regions of the PWN, while spectral indices ~ -0.3 have been associated with the PWN periphery.

7. PWN CONSTRAINTS

As discussed in Section 3.1, the emission at 102 and 213 GHz in the I_{44}−subtracted images appears to peak west of the SN site (Reynolds et al. 1995; Figures 1 and 2), and to mainly extend west of the optical ejecta (see Figure 5). Besides, both the spectral maps and T–T plots (Figures 9 and 10) show that flat spectral indices can be associated with the center–west regions of the SNR (see Section 6). These results could be explained by a possible PWN, powered by a pulsar likely located at a westward offset from the SN position.

The pulsar-kick mechanism has been linked to asymmetries in the core collapse or in the subsequent SN explosion, presumably due to asymmetric mass ejection and/or asymmetric neutrino emission (Podsiadlowski et al. 2005; Wongwathanarat et al. 2013; Nordhaus et al. 2012). As evidence for the natal kick, NS mean three-dimensional (3D) speeds have been estimated at $\overline{v}_{NS} \sim 400 \pm 40$ km s^{-1} (Hobbs et al. 2005), while a transverse velocity of ~ 1083 km s^{-1} has been detected by Chatterjee et al. (2005), which would imply a 3D NS birth velocity as high as 1120 km s^{-1} (Chatterjee et al. 2005). In the context of SNR 1987A, by day 9280 the NS could have travelled westward of the SN site by ~ 20–80 mas, while for an impulsive kick of the same order as $\overline{v}_{NS}$ a distance of $\sim 42 \pm 5$ mas would have been covered. With a western offset of $\sim 0.''05$, the NS would be situated inside the beam of the I_{44}−subtracted images associated with the peak flux density, both at 102 and 213 GHz. If we take into account the ~ 60 mas uncertainty intrinsic to image alignment (see Section 2), as well as the error of 30 mas in each coordinate of the SN VLBI position (Reynolds et al. 1995), the NS could be located near the emission peak as seen in the I_{44}−subtracted images at 102 and 213 GHz. We note that the inner feature of fainter emission detected in the SNR at 44 GHz, as aligned with VLBI observations of the remnant (Zanardo et al. 2013), is centered ~ 60 mas west of the SN site.

If a pulsar is embedded in the unshocked ejecta, the PWN would be in its early stages of evolution, likely surrounded by uniformly expanding gas (Chevalier & Fransson 1992). Diffuse synchrotron emission from the PWN would be due to the relativistic particles, produced by the pulsar, accelerated at the wind termination shock (Kirk et al. 2009).

Assuming a power-law energy distribution of electrons, i.e., the particle density N_e is expressed as $N_e(E) \propto K E^{-s}$, where $s = 1$–2α and $K \propto (m_e c^2)^{s-1}$, the synchrotron emission of the PWN can be written as

$$S_{\nu_P} \propto K\, B_{PWN}^{\frac{1}{2}(s+1)}\, \nu^{\frac{1}{2}(1-s)}, \qquad (7)$$

where B_{PWN} is the nebular magnetic field strength. Noting that, in radio observations, the energy in electrons cannot be separated from that in the magnetic field (Reynolds et al. 2012), the

Table 4
Regional Spectral Indices

Region[c]	Fit[d]	$\alpha_{\rm TT}(S_1, S_2)$[a][e]						$\alpha_{M_\mu}(S_{1,2,3,4})$[b][e]
		(44,102)	(102,213)	(213,345)	(44,94)	(44,213)	(44,345)	(44,94,213,345)
N	y	$\cdots$	$\cdots$	-0.33 ± 0.02	$\cdots$	-0.38 ± 0.03	$\cdots$	$\cdots$
	ODR	$\cdots$	$\cdots$	-0.41 ± 0.02	$\cdots$	$\cdots$	$\cdots$	$\cdots$
	Abs	$\cdots$	$\cdots$	-0.40 ± 0.02	$\cdots$	-0.37 ± 0.03	$\cdots$	$\cdots$
	(0, 0)	$\cdots$	$\cdots$	-0.05 ± 0.04	$\cdots$	-0.43 ± 0.05	$\cdots$	$\cdots$
N1	y	$\cdots$	$\cdots$	$\cdots$	-0.28 ± 0.08	$\cdots$	-0.39 ± 0.02	-0.39 ± 0.09
	ODR	$\cdots$	$\cdots$	$\cdots$	-0.31 ± 0.09	$\cdots$	-0.42 ± 0.02	$\cdots$
	Abs	$\cdots$	$\cdots$	$\cdots$	-0.27 ± 0.08	$\cdots$	-0.35 ± 0.03	$\cdots$
	(0, 0)	$\cdots$	$\cdots$	$\cdots$	-0.36 ± 0.14	$\cdots$	-0.40 ± 0.04	$\cdots$
N2	y	$\cdots$	$\cdots$	$\cdots$	-0.73 ± 0.03	$\cdots$	-0.81 ± 0.08	-0.85 ± 0.14
	ODR	$\cdots$	$\cdots$	$\cdots$	-0.76 ± 0.03	$\cdots$	$\cdots$	$\cdots$
	Abs	$\cdots$	$\cdots$	$\cdots$	-0.77 ± 0.03	$\cdots$	$\cdots$	$\cdots$
	(0, 0)	$\cdots$	$\cdots$	$\cdots$	-0.84 ± 0.04	$\cdots$	-0.89 ± 0.07	$\cdots$
E	y	-0.95 ± 0.02	-0.07 ± 0.02	-1.05 ± 0.04	$\cdots$	-0.48 ± 0.02	$\cdots$	$\cdots$
	ODR	-0.95 ± 0.01	-0.07 ± 0.03	$\cdots$	$\cdots$	-0.60 ± 0.05	$\cdots$	$\cdots$
	Abs	-0.95 ± 0.02	-0.06 ± 0.03	-1.12 ± 0.04	$\cdots$	-0.47 ± 0.02	$\cdots$	$\cdots$
	(0, 0)	-0.97 ± 0.02	-0.03 ± 0.03	0.11 ± 0.07	$\cdots$	-0.46 ± 0.02	$\cdots$	$\cdots$
E0	y	$\cdots$	$\cdots$	$\cdots$	-0.55 ± 0.03	$\cdots$	-0.68 ± 0.03	-0.60 ± 0.03
	ODR	$\cdots$	$\cdots$	$\cdots$	-0.59 ± 0.03	$\cdots$	-0.72 ± 0.04	$\cdots$
	Abs	$\cdots$	$\cdots$	$\cdots$	-0.54 ± 0.03	$\cdots$	-0.66 ± 0.03	$\cdots$
	(0, 0)	$\cdots$	$\cdots$	$\cdots$	-0.69 ± 0.07	$\cdots$	-0.71 ± 0.06	$\cdots$
E1	y	$\cdots$	$\cdots$	$\cdots$	-0.65 ± 0.04	$\cdots$	-0.66 ± 0.04	-0.52 ± 0.13
	ODR	$\cdots$	$\cdots$	$\cdots$	-0.68 ± 0.04	$\cdots$	-0.68 ± 0.04	$\cdots$
	Abs	$\cdots$	$\cdots$	$\cdots$	-0.70 ± 0.05	$\cdots$	-0.65 ± 0.04	$\cdots$
	(0, 0)	$\cdots$	$\cdots$	$\cdots$	-0.78 ± 0.08	$\cdots$	-0.68 ± 0.04	$\cdots$
E2	y	$\cdots$	$\cdots$	$\cdots$	-0.60 ± 0.03	$\cdots$	-0.73 ± 0.03	-0.55 ± 0.12
	ODR	$\cdots$	$\cdots$	$\cdots$	-0.63 ± 0.03	$\cdots$	-0.74 ± 0.02	$\cdots$
	Abs	$\cdots$	$\cdots$	$\cdots$	-0.65 ± 0.03	$\cdots$	-0.72 ± 0.03	$\cdots$
	(0, 0)	$\cdots$	$\cdots$	$\cdots$	-0.74 ± 0.04	$\cdots$	-0.73 ± 0.03	$\cdots$
S	y	$\cdots$	$\cdots$	-0.05 ± 0.05	$\cdots$	-0.45 ± 0.02	$\cdots$	$\cdots$
	ODR	$\cdots$	$\cdots$	-0.10 ± 0.04	$\cdots$	$\cdots$	$\cdots$	$\cdots$
	Abs	$\cdots$	$\cdots$	-0.23 ± 0.03	$\cdots$	-0.44 ± 0.02	$\cdots$	$\cdots$
	(0, 0)	$\cdots$	$\cdots$	-0.22 ± 0.03	$\cdots$	-0.53 ± 0.07	$\cdots$	$\cdots$
S1	y	$\cdots$	$\cdots$	$\cdots$	-0.61 ± 0.02	$\cdots$	-0.52 ± 0.07	-0.63 ± 0.07
	ODR	$\cdots$	$\cdots$	$\cdots$	$\cdots$	$\cdots$	$\cdots$	$\cdots$
	Abs	$\cdots$	$\cdots$	$\cdots$	-0.60 ± 0.02	$\cdots$	-0.56 ± 0.07	$\cdots$
	(0, 0)	$\cdots$	$\cdots$	$\cdots$	-0.95 ± 0.18	$\cdots$	-0.67 ± 0.09	$\cdots$
W	y	-0.77 ± 0.02	-0.11 ± 0.03	0.25 ± 0.04	$\cdots$	-0.40 ± 0.06	$\cdots$	$\cdots$
	ODR	-0.78 ± 0.02	-0.11 ± 0.02	0.17 ± 0.02	$\cdots$	-0.43 ± 0.06	$\cdots$	$\cdots$
	Abs	-0.77 ± 0.02	-0.10 ± 0.03	0.08 ± 0.04	$\cdots$	-0.43 ± 0.06	$\cdots$	$\cdots$
	(0, 0)	-0.76 ± 0.02	-0.18 ± 0.03	0.16 ± 0.03	$\cdots$	-0.49 ± 0.05	$\cdots$	$\cdots$
W0	y	$\cdots$	$\cdots$	$\cdots$	-0.69 ± 0.03	$\cdots$	-0.49 ± 0.09	-0.53 ± 0.05
	ODR	$\cdots$	$\cdots$	$\cdots$	-0.77 ± 0.04	$\cdots$	-0.57 ± 0.10	$\cdots$
	Abs	$\cdots$	$\cdots$	$\cdots$	$\cdots$	$\cdots$	-0.54 ± 0.10	$\cdots$
	(0, 0)	$\cdots$	$\cdots$	$\cdots$	-0.66 ± 0.03	$\cdots$	-0.49 ± 0.11	$\cdots$
W1	y	$\cdots$	$\cdots$	$\cdots$	-0.93 ± 0.09	$\cdots$	-0.61 ± 0.09	-0.37 ± 0.11
	ODR	$\cdots$	$\cdots$	$\cdots$	-0.97 ± 0.08	$\cdots$	$\cdots$	$\cdots$
	a	$\cdots$	$\cdots$	$\cdots$	-0.99 ± 0.08	$\cdots$	-0.60 ± 0.09	$\cdots$
	(0, 0)	$\cdots$	$\cdots$	$\cdots$	-0.75 ± 0.10	$\cdots$	-0.51 ± 0.15	$\cdots$
W2	y	$\cdots$	$\cdots$	$\cdots$	-0.40 ± 0.11	$\cdots$	-0.50 ± 0.02	-0.47 ± 0.11
	ODR	$\cdots$	$\cdots$	$\cdots$	-0.44 ± 0.11	$\cdots$	-0.52 ± 0.02	$\cdots$
	Abs	$\cdots$	$\cdots$	$\cdots$	-0.35 ± 0.12	$\cdots$	-0.49 ± 0.02	$\cdots$
	(0, 0)	$\cdots$	$\cdots$	$\cdots$	-0.52 ± 0.14	$\cdots$	-0.51 ± 0.02	$\cdots$
C	y	-0.86 ± 0.08	-0.00 ± 0.04	1.20 ± 0.04	$\cdots$	-0.43 ± 0.02	$\cdots$	$\cdots$
	ODR	-0.90 ± 0.08	-0.00 ± 0.03	1.97 ± 0.09	$\cdots$	$\cdots$	$\cdots$	$\cdots$
	Abs	-0.86 ± 0.08	-0.00 ± 0.03	2.25 ± 0.11	$\cdots$	-0.44 ± 0.01	$\cdots$	$\cdots$
	(0, 0)	-0.84 ± 0.08	-0.09 ± 0.04	$\cdots$	$\cdots$	-0.43 ± 0.02	$\cdots$	$\cdots$
C1	y	$\cdots$	$\cdots$	$\cdots$	-0.40 ± 0.08	$\cdots$	$\cdots$	-0.01 ± 0.06
	ODR	$\cdots$	$\cdots$	$\cdots$	$\cdots$	$\cdots$	$\cdots$	$\cdots$
	Abs	$\cdots$	$\cdots$	$\cdots$	-0.47 ± 0.08	$\cdots$	$\cdots$	$\cdots$
	(0, 0)	$\cdots$	$\cdots$	$\cdots$	-0.73 ± 0.15	$\cdots$	$\cdots$	$\cdots$

Notes.

[a] The spectral indices $\alpha_{\rm TT}$ are derived from five images at 44, 94, 102, 213, and 345 GHz. The images are analyzed in six frequency pairs, as indicated in Figure 10.

[b] The median spectral index, α_{M_μ}, is derived by fitting a Gaussian to the histogram of the α_M values resulting in the spectral map obtained from images at 44, 94, 213, and 345 GHz in the corresponding T–T region (see the top map in Figure 10).

[c] The regions selected for the T–T plots are designated in Figure 10.

[d] The given spectral indices are derived from different linear interpolations: least-square fit from vertical squared errors, α_y; orthogonal distance regression, $\alpha_{\rm ODR}$; robust fitting from the square root of absolute residuals, $\alpha_{\rm Abs}$; linear regression with forced zero interception ($S_1 = 0$, $S_2 = 0$), $\alpha_{(0, 0)}$.

[e] The errors on $\alpha_{\rm TT}$ and α_{M_μ} are the 1σ error on the slope of the linear fit combined with the uncertainty in the flux calibration.

equipartition magnetic-field strength could be derived as (e.g., Longair 2011; see revised formula by Beck & Krause 2005; Arbutina et al. 2012)

$$B_{\mathrm{PWN}} \approx \left[G_0\, G\, (\mathcal{K}+1)\, \frac{S_\nu}{f\, d\, \theta_{\mathrm{PWN}}^3}\, \nu^{\frac{(1-s)}{2}} \right]^{\frac{2}{(5+s)}},\qquad (8)$$

where G_0 is a constant, $G = G(\nu, s)$ is the product of different functions varying with the minimum and maximum frequencies associated with the spectral component and the synchrotron spectral index (Beck & Krause 2005; Longair 2011), $\mathcal{K}$ is the ion/electron energy ratio, f is the volume filling factor of radio emission, and $\theta_{\mathrm{PWN}} = R_{\mathrm{PWN}}/d$ is the angular radius. Considering $0.''05 \lesssim R_{\mathrm{PWN}} \lesssim 0.''15$, $-0.4 \leqslant \alpha \leqslant -0.1$ (as from Section 5), $102 \leqslant \nu \leqslant 672\,\mathrm{GHz}$, $S_\nu \approx 3\,\mathrm{mJy}$, and taking $\mathcal{K} \approx 100$ (Beck & Krause 2005) while $f \approx 0.5$, Equation (8) leads to $1 \lesssim B_{\mathrm{PWN}} \lesssim 7\,\mathrm{mG}$. For $0.2 \lesssim f \lesssim 0.9$, $2 \lesssim B_{\mathrm{PWN}} \lesssim 5\,\mathrm{mG}$. Since the equipartition is a conjecture for young SNRs and no longer valid when the spectral index is flatter than -0.5, these B_{PWN} estimates might be inaccurate.

The energy inside the PWN, due to the PWN magnetic field, can be simplified as

$$E_{\mathrm{PWN},B}(t) \sim V_{\mathrm{PWN}}(t)\frac{B_{\mathrm{PWN}}^2}{8\pi},\qquad (9)$$

where the magnetic field is considered uniform and isotropic inside the PWN volume, $V_{\mathrm{PWN}}(t) = 4/3\,\pi\,R_{\mathrm{PWN}}^3(t)$. For $0.''05 \lesssim R_{\mathrm{PWN}} \lesssim 0.''15$, and, as for the parameters used in Equation (8), $1 \lesssim B_{\mathrm{PWN}} \lesssim 7\,\mathrm{mG}$, at $t = t_{25} = 8.0 \times 10^8\,\mathrm{s}$ ($\approx 9280\,\mathrm{days}$), we estimate $0.9 \times 10^{43} \lesssim E_{\mathrm{PWN},B} \lesssim 1.2 \times 10^{46}\,\mathrm{erg}$. According to models by Chevalier & Fransson (1992), about 30% of the total energy input into the PWN, E_{PWN}, goes to the internal magnetic pressure in the PWN, while most of the remaining pulsar spin-down energy would drive the PWN expansion into the ejecta.

In terms of integrated radio luminosity, calculated as

$$L_{\mathrm{rad}}(\nu) = 4\pi d^2 \int_{\nu_{\mathrm{min}}}^{\nu_{\mathrm{max}}} S_\nu(\nu)\, d\nu,\qquad (10)$$

if $\nu_{\mathrm{min}} = 102\,\mathrm{GHz}$ and $\nu_{\mathrm{max}} = 672\,\mathrm{GHz}$ bracket the frequency range in which the PWN is detected, $S_\nu \approx 3\,\mathrm{mJy}$ leads to $L_{\mathrm{rad}} \approx 5.4 \times 10^{33}\,\mathrm{erg\,s^{-1}}$. The derived L_{rad} is comparable with the limit of $L_{\mathrm{opt}} \leqslant 5 \times 10^{33}\,\mathrm{erg\,s^{-1}}$ given by Graves et al. (2005) for a compact source in the optical band from 290 to 965 nm at $t = 6110$ days. A similar limit has been placed on the 2–10 keV X-ray luminosity, $L_X \leqslant 5.5 \times 10^{33}\,\mathrm{erg\,s^{-1}}$, using *Chandra* images (Park et al. 2004). Since these L_ν estimates are upper limits and free–free emission may be a substantial component of the radio luminosity (see Section 5.1), we can take $L_{\mathrm{rad}} \approx 10^{33}\,\mathrm{erg\,s^{-1}}$ as a realistic upper limit.

In the free-expansion regime (Chevalier & Fransson 1992), $\sim 1\%$ of the pulsar power is emitted by the shock wave in the SN and additional emission from the pulsar nebula is expected. Given this, we can set $\dot{E}_{\mathrm{spin}} \approx 10^{35}\,\mathrm{erg\,s^{-1}}$ as an upper limit for the spin-down power of the pulsar. For a typical pulsar surface dipole magnetic field $B_s \sim 10^{12}\,\mathrm{G}$ (Manchester et al. 2005b), this spin-down luminosity corresponds to a pulsar period $P \sim 0.15\,\mathrm{s}$ and characteristic age $\tau_c = P/(2\dot{P}) \sim 10^5$ years. Lower luminosities would imply lower dipole magnetic fields and/or longer pulsar periods. Such parameter ranges are plausible for the putative pulsar at the center of SN 1987A, as there is good
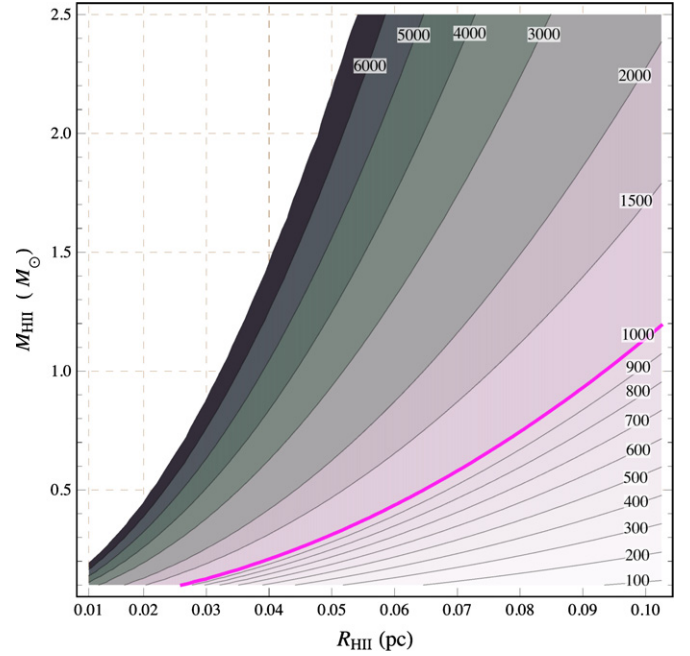
Figure 12. Dispersion measure (DM) associated with a possible pulsar in SNR 1987A, assuming an ionized fraction of the ejecta $0.1\,M_\odot \lesssim M_{\mathrm{HII}} \lesssim 2.5\,M_\odot$, uniformly distributed within a spherical region with radius $0.01 \lesssim R_{\mathrm{H\,II}} \lesssim 0.10$ pc (i.e., $0.''05 \lesssim R_{\mathrm{H\,II}} \lesssim 0.''42$). The color scheme changes from white to black for increasing DM values, which range from 100 to 6000 cm^{-3} pc, as indicated by the contour labels. The contour at DM $=1000$ cm^{-3} pc is highlighted in magenta.

(A color version of this figure is available in the online journal.)

evidence that many pulsars are born with a spin period not much different to their present period (Popov & Turolla 2012; Gotthelf et al. 2013).

Following Chevalier (1977), the velocity at the outer edge of the nebula can be defined as

$$v_{\mathrm{PWN}} = \frac{6}{5}\left(\frac{125}{132}\, \frac{\dot{E}_{\mathrm{spin}}\, t}{\pi \rho_{ej}\, t^3} \right)^{\frac{1}{5}},\qquad (11)$$

assuming the PWN is freely expanding and has constant density ρ_{ej}. At $t = t_{25}$, setting $10^{-18} \lesssim \rho_{ej} \lesssim 10^{-19}\,\mathrm{g\,cm^{-3}}$ in the central region of the SNR, as from the density model by Blinnikov et al. (2000; see Figure 21 in Fransson et al. 2013), the swept-up shell velocity becomes $260 \lesssim v_{\mathrm{PWN}} \lesssim 410\,\mathrm{km\,s^{-1}}$, which leads to R_{PWN} not greater than $0.''05$. Since this is well below the resolution of the ATCA and ALMA images presented here, the emission from a possible PWN would appear as a point source.

As mentioned in Section 5, a pulsar embedded in the SNR interior would emit ionizing radiation within the inner layers of the ejecta. While an X-ray pulsar has yet to be detected (Helder et al. 2013), illumination of the inner ejecta by X-ray flux has been reported by Larsson et al. (2011) though attributed to the reverse and reflected shocks, as well as to shocks propagating into the ER.

Given the early stages of a possible PWN, the ionized ejecta would be mainly due to the radiation from the various shocks. If the H$_{\mathrm{II}}$ region is assumed to be spherical (see Section 5), the related dispersion measure (DM) can be derived as $\mathrm{DM}(M_{\mathrm{H\,II}}, R_{\mathrm{H\,II}}) \approx 3\,M_{\mathrm{H\,II}}/(m_p\, 4\pi\, R_{\mathrm{H\,II}}^2)$. Neglecting clumping in the ejecta, for $0.1\,M_\odot \lesssim M_{\mathrm{H\,II}} \lesssim 2.5\,M_\odot$ and $0.01 \lesssim R_{\mathrm{H\,II}} \lesssim 0.10$ pc (i.e., $0.''05 \lesssim R_{\mathrm{H\,II}} \lesssim 0.''42$), the resulting DM is shown in Figure 12.

8. CONCLUSIONS

We have presented a comprehensive morphological and spectral analysis of SNR 1987A based on both ATCA and ALMA data (Cycle 0), from 1.4 to 672 GHz. We have investigated the components of the SNR emission across the transition from radio to FIR, as the combination of non-thermal and thermal emission. A summary of our findings is as follows.

1. To decouple the non-thermal emission from that originating from dust, the synchrotron component, as resolved with ATCA at 44 GHz, and the dust component, as imaged with ALMA at 672 GHz, were subtracted from the data sets at 94, 102, 213, 345, and 672 GHz. The images derived from the subtraction of the scaled model flux density at 672 GHz, highlight the ring-like synchrotron emission that originates over the ER. The images similarly obtained from the subtraction of the 44 GHz model, show residual emission mainly localized west of the SN site.

2. An analysis of the emission distribution over the ER, in images from 44 to 345 GHz, shows a gradual decrease of the east-to-west asymmetry ratio with frequency. We attribute this to the shorter synchrotron lifetime at high frequencies. We estimate that, at frequencies higher than 213 GHz, the electrons might be unable to cross the eastern emission region.

3. Across the transition from radio to FIR, the SED suggests additional emission components beside the synchrotron main component ($S_\nu \propto \nu^{-0.73}$) and the thermal emission originating from dust grains at $T \sim 22$ K. We argue that this excess emission could be due to a second flat-spectrum synchrotron component with $-0.4 \lesssim \alpha \lesssim -0.1$. This could imply the presence of a PWN originating from an embedded pulsar.

4. Spectral index measurements across the SNR, from 44 to 345 GHz, show predominantly flat spectral indices, $-0.4 \lesssim \alpha \lesssim -0.1$, in the western half of the remnant at frequencies above 102 GHz, while $\alpha \sim 0$ around the central region. From 102 to 213 GHz, $-0.1 \lesssim \alpha \lesssim 0$ across the whole remnant. From 213 to 345 GHz, the steepening of the spectral indices over the eastern lobe might be indication of a local spectral break.

5. Results from both the morphological and spectral analysis might suggest the presence of a PWN in the SNR interior, powered by a pulsar likely located at a westward offset from the SN position. In this scenario, a NS embedded in the unshocked ejecta might be emitting diffuse synchrotron emission $S_{\nu_P} \sim 3$ mJy above 102 GHz. The possible PWN would have magnetic field strength $1 \lesssim B_{\mathrm{PWN}} \lesssim 7$ mG. The upper limit of the integrated radio luminosity is derived as $L_{\mathrm{rad}} \sim 5.4 \times 10^{33}$ erg s^{-1}, which leads to an upper limit of the pulsar spin-down power $\dot{E}_{\mathrm{spin}} \approx 10^{35}$ erg s^{-1}. While effects such as luminosity, beaming, scattering, and absorption might have prevented the detection of pulsed emission in the SNR for over 20 years (Manchester 1988, 2007), a renewed pulsar search with the *Parkes* telescope is currently in progress. Future observations with ALMA, ATCA and VLBI are needed to probe the SNR for a possible PWN.

REFERENCES

Arbutina, B., Urošević, D., Andjelić, M. M., Pavlović, M. Z., & Vukotić, B. 2012, ApJ, 746, 79
Arendt, R. G., George, J. V., Staguhn, J. G., et al. 2011, ApJ, 734, 54
Ball, L., Crawford, D. F., Hunstead, R. W., Klamer, I., & McIntyre, V. J. 2001, ApJ, 549, 599
Beck, R., & Krause, M. 2005, AN, 326, 414
Bell, A. R. 2004, MNRAS, 353, 558
Bell, A. R., & Lucek, S. G. 2001, MNRAS, 321, 433
Berezhko, E. G., & Ksenofontov, L. T. 2006, ApJL, 650, L59
Berezhko, E. G., Ksenofontov, L. T., & Völk, H. J. 2011, ApJ, 732, 58
Bionta, R. M., Blewitt, G., Bratton, C. B., Casper, D., & Ciocio, A. 1987, PhRvL, 58, 1494
Blinnikov, S., Lundqvist, P., Bartunov, O., Nomoto, K., & Iwamoto, K. 2000, ApJ, 532, 1132
Blondin, J. M., & Lundqvist, P. 1993, ApJ, 405, 337
Borkowski, K. J., Blondin, J. M., & McCray, R. 1997, ApJ, 477, 281
Bouchet, P., Dwek, E., Danziger, J., et al. 2006, ApJ, 650, 212
Briggs, D. S. 1995, BAAS, 27, 1444
Chatterjee, S., Vlemmings, W. H. T., Brisken, W. F., et al. 2005, ApJL, 630, L31
Chevalier, R. A. 1977, in Supernovae, ed. D. N. Schramm (Astrophysics and Space Science Library, Vol. 66; Berlin: Springer), 53
Chevalier, R. A. 1982, ApJ, 259, 302
Chevalier, R. A., & Dwarkadas, V. V. 1995, ApJL, 452, L45
Chevalier, R. A., & Fransson, C. 1992, ApJ, 395, 540
Condon, J. J. 1992, ARA&A, 30, 575
Cortese, L., Fritz, J., Bianchi, S., et al. 2014, MNRAS, 440, 942
Costain, C. H. 1960, MNRAS, 120, 248
Crotts, A. P. S., & Heathcote, R. S. 2000, ApJ, 528, 426
Dwek, E., Arendt, R. G., Bouchet, P., et al. 2010, ApJ, 722, 425
Fransson, C., Larsson, J., Spyromilio, J., et al. 2013, ApJ, 768, 88
Gaensler, B. M., Manchester, R. N., Staveley-Smith, L., et al. 1997, ApJ, 479, 845
Gaensler, B. M., & Slane, P. O. 2006, ARA&A, 44, 17
Gaensler, B. M., Staveley-Smith, L., Manchester, R. N., et al. 2007, in AIP Conf. Proc. 937, Supernova 1987A: 20 Years After: Supernovae and Gamma-Ray Bursters, ed. S. Immler, K. W. Weiler, & R. McCray (Melville, NY: AIP), 86
Gotthelf, E. V., Halpern, J. P., & Alford, J. 2013, ApJ, 765, 58
Graves, G. J. M., Challis, P. M., Chevalier, R. A., et al. 2005, ApJ, 629, 944
Green, D. A. 2011, BASI, 39, 289
Glushkov, A. V., Ksenofontov, L. T., & Pravdin, M. I. 2013, JPhCS, 409, 012069
Gull, S. F., & Daniell, G. J. 1978, Natur, 272, 686
Haines, T., Bratton, C. B., Casper, D., et al. 1988, NIMPA, 264, 28
Helder, E. A., Broos, P. S., Dewey, D., et al. 2013, ApJ, 764, 11
Hillebrandt, W., Höflich, P., Truran, J. W., & Weiss, A. 1987, Natur, 327, 597
Hirata, K., Kajita, T., Koshiba, M., Nakahata, M., & Oyama, Y. 1987, PhRvL, 58, 1490
Hobbs, G., Lorimer, D. R., Lyne, A. G., & Kramer, M. 2005, MNRAS, 360, 974
Högbom, J. H. 1974, A&AS, 15, 417
Indebetouw, R., Matsuura, M., Dwek, E, et al. 2014, ApJL, 782, L2 (I14)
Jakobsen, P., Albrecht, R., Barbieri, C., et al. 1991, ApJL, 369, L63
Kamenetzky, J., McCray, R., Indebetouw, R., et al. 2013, ApJL, 773, L34
Kozma, C., & Fransson, C. 1998, ApJ, 497, 431
Kirk, J. G., Duffy, P., & Gallant, Y. A. 1996, A&A, 314, 1010
Kirk, J. G., Lyubarsky, Y., & Petri, J. 2009, in Neutron Stars and Pulsars, ed. W. Becker (Astrophysics and Space Science Library, Vol. 357; Berlin: Springer), 421

Kjær, K., Leibundgut, B., Fransson, C., Jerkstrand, A., & Spyromilio, J. 2. 2010, A&A, 517, A51

Lakićević, M., van Loon, J. Th., Patat, F., Staveley-Smith, L., & Zanardo, G. 2011, A&A, 532, L8

Lakićević, M., van Loon, J. Th., Stanke, T., De Breuck, C., & Patat, F. 2012a, A&A, 541, L1

Lakićević, M., Zanardo, G., van Loon, J. Th., et al. 2012b, A&A, 541, L2

Larsson, J., Fransson, C., Kjær, K., et al. 2013, ApJ, 768, 89

Larsson, J., Fransson, C., Östlin, G., et al. 2011, Natur, 474, L484

Longair, M. S. 2011, High Energy Astrophysics 2011 (Cambridge: Cambridge University Press), 550

Manchester, R. N. 1988, PASA, 7, 548

Manchester, R. N. 2007, in AIP Conf. Proc. 937, Supernova 1987A: 20 Years After: Supernovae and Gamma-Ray Bursters, ed. S. Immler, K. W. Weiler, & R. McCray (Melville, NY: AIP), 134

Manchester, R. N., Gaensler, B. M., Staveley-Smith, L., Kesteven, M. J., & Tzioumis, A. K. 2005a, ApJL, 628, L131

Manchester, R. N., Gaensler, B. M., Wheaton, V. C., et al. 2002, PASA, 19, 207

Manchester, R. N., Hobbs, G. B., Teoh, A., & Hobbs, M. 2005b, AJ, 129, 1993

Martin, C. L., & Arnett, D. 1995, ApJ, 447, 378

Matsuura, M., Dwek, E., Barlow, M. J., et al. 2014, ApJ, submitted

Matsuura, M., Dwek, E., Meixner, M., et al. 2011, Sci, 333, 1258

Morris, T., & Podsiadlowski, P. 2007, Sci, 315, 1103

Morris, T., & Podsiadlowski, P. 2009, MNRAS, 399, 515

Ng, C.-Y., Gaensler, B. M., Staveley-Smith, L., et al. 2008, ApJ, 684, 481

Ng, C.-Y., Potter, T. M., Staveley-Smith, L., et al. 2011, ApJL, 728, L15

Ng, C.-Y., Zanardo, G., Potter, T. M., et al. 2013, ApJ, 777, 131

Nordhaus, J., Brandt, T. D., Burrows, A., & Almgren, A. 2012, MNRAS, 423, 1805

Park, S., Zhekov, S. A., Burrows, D. N., Garmire, G. P., & McCray, R. 2004, ApJ, 610, 275

Park, S., Zhekov, S. A., Burrows, D. N., & McCray, R. 2005, ApJL, 634, L73

Park, S., Zhekov, S. A., Burrows, D. N., et al. 2006, ApJ, 646, 1001

Plait, P. C., Lundqvist, P., Chevalier, R. A., & Kirshner, R. P. 1995, ApJ, 439, 730

Podsiadlowski, P., Pfahl, E., & Rappaport, S. 2005, in ASP Conf. Ser. 328, Binary Radio Pulsars, ed. F. A. Rasio & I. H. Stairs (San Francisco, CA: ASP), 327

Popov, S. B., & Turolla, R. 2012, Ap&SS, 341, 457

Potter, T. M., Staveley-Smith, L., Ng, C.-Y., et al. 2009, ApJ, 705, 261

Racusin, J. L., Park, S., Zhekov, S., et al. 2009, ApJ, 703, 1752

Reynolds, J. E, Jauncey, D. L., Staveley-Smith, L., et al. 1995, A&A, 304, 116

Reynolds, S. P., Gaensler, B. M., & Bocchino, F. 2012, SSRv, 166, 231

Rybicki, G. B., & Lightman, A. P. 1979, Radiative Processes in Astrophysics (New York: Wiley), 162

Smartt, S. J. 2009, ARA&A, 47, 63

Staveley-Smith, L., Briggs, D. S., Rowe, A. C. H., et al. 1993, Natur, 366, 136

Staveley-Smith, L., Manchester, R. N., Kesteven, M. J., et al. 1992, Natur, 355, 147

Staveley-Smith, L., Potter, T. M., Zanardo, G., Gaensler, B. M., & Ng, C.-Y. 2014, in IAU Symp. 296, Supernova Environmental Impacts (Cambridge: Cambridge Univ. Press), 15

Storey, P. J., & Hummer, D. G. 1995, MNRAS, 272, 41

Thielemann, F. K., & Arnett, W. D. 1985, ApJ, 295, 604

Turtle, A. J., Campbell-Wilson, D., Manchester, R. N., Staveley-Smith, L., & Kesteven, M. J. 1990, IAUC, 5086, 2

Turtle, A. J., Pugh, J. F., Kenderdine, S., & Pauliny-Toth, I. I. K. 1962, MNRAS, 124, 297

Tziamtzis, A., Lundqvist, P., Gröningsson, P., & Nasoudi-Shoar, S. 2011, A&A, 527, 35

Wongwathanarat, A., Janka, H.-Th., & Mller, E. 2013, A&A, 552, 126

Zanardo, G., Staveley-Smith, L., Ball, L., et al. 2010, ApJ, 710, 1515

Zanardo, G., Staveley-Smith, L., Ng, C.-Y., et al. 2013, ApJ, 767, 98

Zhekov, S. A., McCray, R., Dewey, D., et al. 2009, ApJ, 692, 1190

Zhekov, S. A., Park, S., McCray, R., Racusin, J. L., & Burrows, D. N. 2010, MNRAS, 407, 1157

Zubko, V. G., Dwek, E., & Arendt, R. G. 2004, ApJS, 152, 211

Zubko, V. G., Mennella, V., Colangeli, L., & Bussoletti, E. 1996, MNRAS, 282, 1321